

Constraining Galaxy-Halo Connection Using Machine Learning

Abhishek Jana^{a,*}, Lado Samushia^{a,b,c}

^aDepartment of Physics, Kansas State University, 116 Cardwell Hall, Manhattan, 66502, KS, USA

^bE.Kharadze Georgian National Astrophysical Observatory, 47/57 Kostava St., Tbilisi, 0179, Georgia

^cSchool of Natural Sciences and Medicine, Ilia State University, 3/5 Cholokashvili Ave., Tbilisi, 0162, Georgia

Abstract

We investigate the potential of machine learning (ML) methods to model small-scale galaxy clustering for constraining Halo Occupation Distribution (HOD) parameters. Our analysis reveals that while many ML algorithms report good statistical fits, they often yield likelihood contours that are significantly biased in both mean values and variances relative to the true model parameters. This highlights the importance of careful data processing and algorithm selection in ML applications for galaxy clustering, as even seemingly robust methods can lead to biased results if not applied correctly. ML tools offer a promising approach to exploring the HOD parameter space with significantly reduced computational costs compared to traditional brute-force methods if their robustness is established. Using our ANN-based pipeline, we successfully recreate some standard results from recent literature. Properly restricting the HOD parameter space, transforming the training data, and carefully selecting ML algorithms are essential for achieving unbiased and robust predictions. Among the methods tested, artificial neural networks (ANNs) outperform random forests (RF) and ridge regression in predicting clustering statistics, when the HOD prior space is appropriately restricted. We demonstrate these findings using the projected two-point correlation function ($w_p(r_p)$), angular multipoles of the correlation function ($\xi_\ell(r)$), and the void probability function (VPF) of Luminous Red Galaxies from Dark Energy Spectroscopic Instrument mocks. Our results show that while combining $w_p(r_p)$ and VPF improves parameter constraints, adding the multipoles ξ_0 , ξ_2 , and ξ_4 to $w_p(r_p)$ does not significantly improve the constraints.

Keywords: large-scale structure of Universe, galaxies: halos, cosmology: theory, methods: machine learning

1. Introduction

Clustering of matter on small scales due to gravitational instability is a highly non-linear process that can only be solved by running time-consuming N-body simulations. The N-body simulations trace the evolution of a large number of dark matter particles over cosmic times. They can be used to study the gravitational collapse of dark matter particles into virialized halos. Multiple high-performance N-body simulation codes are available that allow us to study the clustering properties of halos, the distribution of their properties, and the distribution of dark matter inside them, with a sub-percent precision (Springel et al., 2001; Teyssier, 2002; Springel, 2005; Ishiyama et al., 2009; Springel, 2010; Bédorf et al., 2012; Angulo et al., 2012; Fosalba et al., 2015; Klypin et al., 2016; Dubois et al., 2016; Potter et al., 2017; DeRose et al., 2019; Heitmann et al., 2019; Springel et al., 2021; Maksimova et al., 2021).

The creation of galaxies inside dark matter halos is a more complicated process, requiring us to keep track of multiple intricate baryonic processes occurring during galaxy formation and evolution. Even though several codes for simulating these baryonic processes are available, they are much more computationally demanding (Dubois et al., 2014; Schaye et al., 2015;

Nelson et al., 2015; McCarthy et al., 2017; Davé et al., 2019; Nelson et al., 2019). The best current pure dark matter N-body simulations have cumulative volumes of up to (11.19 Gpc)³, while the best simulations with baryons in them have only (740 Mpc)³.

One way to circumvent this problem is to populate the N-body simulations with galaxies based on a simplified prescription. One such approach is the Halo Occupation Distribution (HOD) (Jing et al., 1998; Seljak, 2000; Peacock and Smith, 2000; Scoccimarro et al., 2001; Berlind and Weinberg, 2002; Cooray and Sheth, 2002; Zheng et al., 2005, 2007, 2009). The main assumption of the HOD approach is that the average properties of galaxies depend on their local environment. In the simplest version of the HOD, we put galaxies into dark matter halos based on the host halo mass. The host halo mass determines the probability of that halo hosting a central galaxy and a certain number of satellite galaxies. The velocities and positions of those galaxies are similarly determined. The exact dependence of these probabilities on the halo mass is tuned to match the observed clustering of galaxies. More advanced HOD prescriptions will also make the probabilities depend on other properties of the local neighborhood, like the local density of halos. These extra dependencies, collectively known as the assembly bias, have been shown to be important in the simulations (Zehavi et al., 2018; Artale et al., 2018; Bose et al., 2019; Alfaro et al., 2020, 2021), but have not been convincingly detected in

*Corresponding author

Email addresses: ajana@ksu.edu (Abhishek Jana), lado@ksu.edu (Lado Samushia)

real data (Alfaro et al., 2022).

To derive cosmological constraints from small-scale clustering we need to marginalize all possible HOD parameters that are consistent with the data at a given cosmology. This process could be very time-consuming. The space of HOD parameters is at least five dimensional and the statistics used to describe small-scale clustering are time-consuming to compute. One way to speed up the process that is becoming popular is to use machine learning to predict clustering as a function of HOD parameters.

The use of machine learning (ML) methods to predict cosmological observables is currently a very popular direction of research. The artificial neural networks (ANN) have been used in Agarwal et al. (2018); Gómez-Vargas et al. (2021); Nygaard et al. (2023); Perez et al. (2023) to efficiently model galaxy-halo properties, emulate cosmological calculations, and constrain cosmological parameters. Recent works on deriving HOD constraints using ML methods mostly focus on methods like Symbolic Regression, Random Forest Regression, k-nearest-neighbors (Xu et al., 2013; Ntampaka et al., 2020; Wadekar et al., 2020; Xu et al., 2021; Delgado et al., 2022; Dumerchat and Bautista, 2023).

In this work, we will train ANN so that they can predict the values of key clustering measures as functions of the HOD parameters. This enables us to run Markov Chain Monte Carlo (MCMC) over the HOD parameters that converge in a few minutes, whereas a brute force approach would take several days. We also investigate the potential of other ML techniques like random forests (RF), and Bayesian ridge (BR) to accelerate HOD modeling. We focus on modeling two well-known clustering metrics – the projected two-point correlation function $w_p(r_p)$ and the void probability function VPF measured from mock galaxy catalogs. We also measured monopole (ξ_0), quadrupole (ξ_2), and hexadecapole (ξ_4) to compare with $w_p(r_p)$. Our goal is to train ML algorithms to rapidly predict these clustering signals for any point in HOD parameter space.

2. Creating Mock Galaxy Catalogs

To create mock galaxy catalogs from N-body simulations we perform steps described in the following subsections.

2.1. Simulation Details

For our analysis, we use the AbacusSummit_base_c132_ph000 broader emulator grid of AbacusSummit¹ N-body simulation suite (Metchnik, 2009; Garrison et al., 2019, 2021, 2018; Garrison et al., 2016). The simulation is conducted in a flat Λ CDM cosmology characterized by the following parameters: $\omega_b = 0.02237$, $\omega_{\text{cdm}} = 0.1200$, $h = 0.6736$, $A_s = 2.1791 \times 10^{-9}$, and $n_s = 0.9049$. The simulation box has a side length of $2000h^{-1}$ Mpc and contains 6912^3 particles, totaling approximately 330 billion particles, with a particle mass of about $2 \times 10^9 M_\odot/h$.

¹<https://abacussummit.readthedocs.io/en/latest/>

Our study specifically focuses on box number 132 within this simulation suite, corresponding to a redshift of $z = 1.1$. We populate this box with galaxies using the HOD model, with parameters listed in Table 1. These galaxies are used for subsequent clustering analyses as part of our broader study of large-scale structures.

2.2. HOD Model

We follow the HOD approach to create galaxy catalogs out of the AbacusSummit simulation. Given a halo mass (M_{halo}), this model specifies the probability of central (N_{cen}) and satellite (N_{sat}) galaxies. We will use a simple implementation of this idea where the probabilities only depend on the halo mass (M_{halo}). We consider central and satellite separately as central galaxies reside in the potential well of the host halo and satellite galaxies follow different physics for their formation. The mean occupation function of the central galaxy $\langle N_{\text{cen}}(M_{\text{halo}}) \rangle$ is a step-like function with a characteristic minimum halo mass M_{cut} , and the mean occupation function of the central galaxy $\langle N_{\text{sat}}(M_{\text{halo}}) \rangle$ follows a power law with index α and characteristic satellite mass M_1 . For Luminous Red Galaxies (LRG), the HOD model is defined as a five-parameter model (Alam et al., 2020) with the average number density $\langle N(M_{\text{halo}}) \rangle$ of a specific halo mass M_{halo} is given by

$$\langle N(M_{\text{halo}}) \rangle = \langle N_{\text{cen}}(M_{\text{halo}}) \rangle + \langle N_{\text{sat}}(M_{\text{halo}}) \rangle, \quad (1)$$

where,

$$\langle N_{\text{cen}}(M_{\text{halo}}) \rangle = \frac{1}{2} p_{\text{max}} \operatorname{erfc} \left(\frac{\log_{10} M_{\text{cut}} - \log_{10} M_{\text{halo}}}{\sqrt{2} \log_{10}(e) \sigma_{\text{M}}} \right), \quad (2)$$

$$\langle N_{\text{sat}}(M_{\text{halo}}) \rangle = \mathcal{H} \left(\frac{M_{\text{halo}}}{\kappa M_{\text{cut}}} \right) \left(\frac{M_{\text{halo}} - \kappa M_{\text{cut}}}{M_1} \right)^\alpha \langle N_{\text{cen}}(M_{\text{halo}}) \rangle, \quad (3)$$

where,

$$\mathcal{H} \left(\frac{M_{\text{halo}}}{\kappa M_{\text{cut}}} \right) = \begin{cases} 1, & M_{\text{halo}} > \kappa M_{\text{cut}} \\ 0, & \text{otherwise.} \end{cases} \quad (4)$$

Here p_{max} is the saturation level that controls the probability of hosting a central galaxy. For Luminous Red Galaxy (LRG) only samples, p_{max} is set to 1 meaning that most of the massive halos are guaranteed to possess a central galaxy. M_{cut} is the characteristic minimum mass of the halos to host a central galaxy and the quantity σ_{M} changes the shape of the ‘‘central galaxy probability function’’, by controlling the sharpness of the transition around M_{cut} . Higher σ_{M} means a smoother transition between 0 and 1 occupation probabilities.

Three additional parameters κ , α , and M_1 are used to get satellite probability. M_1 is the characteristic satellite mass, α is the power law index of the satellite distribution and κ determines the cut-off mass in the units of M_{cut} .

2.3. Galaxy Catalogs

We generate 20,000 sets of HOD parameters by randomly selecting them within the bounds in Table 1 labeled as the “full box”, with uniform probability. We discard the HOD parameter sets that result in a galaxy sample with a density of less than $\bar{n} = 4.25 \times 10^{-4} h^3 \text{ Mpc}^{-3}$. At these low number densities, the clustering measurements become very noisy, making it difficult to obtain reliable interpolations. The main galaxy samples relevant for cosmological analysis from large spectroscopic surveys, either currently available or expected soon (such as the baryon oscillations spectroscopic survey (Dawson et al., 2013), dark energy spectroscopic survey (DESI Collaboration et al., 2016), Euclid satellite mission (Euclid Collaboration et al., 2022), Roman space telescope (Spergel et al., 2015)) have number densities that are larger than our thresholds. Computing clustering measurements from a very large number of galaxies is time-consuming. To avoid extremely large computational times, we decided to also discard the HOD parameter sets that result in a sample with a density higher than $\bar{n} = 1.75 \times 10^{-2} h^3 \text{ Mpc}^{-3}$. Both of these extreme number densities are sufficiently far away from the samples obtained in realistic galaxy surveys to be of practical importance. After imposing additional cuts on the number density we are left with 8,337 mocks out of 20,000.

To achieve more reliable interpolation over a smaller parameter space, we separately generate 6,000 galaxy samples within tighter HOD parameter bounds. This reduced parameter range is labeled as the “small box” in Table 1. The range is chosen in such a way that the galaxy number density is always well within the above-mentioned range of $4.25 \times 10^{-4} h^3 \text{ Mpc}^{-3} < \bar{n} < 1.75 \times 10^{-2} h^3 \text{ Mpc}^{-3}$.

The full box covers a very wide range of possible HOD parameter values that can describe all the galaxy samples from current and future surveys relevant to cosmological analysis. The small box covers a range of values that is smaller than what the current precision of clustering measurements allows. We expect the interpolation within the small box to be much more reliable. We will see in the Section 6.3 however even within the small box the interpolation sometimes runs into serious problems. The size of the small box that is safe enough for interpolation will likely change for extended HOD models. Grey points on Fig. 1 shows the HOD parameter values used in this work. The outer edges of the plots correspond to the full box cuts, while the smaller red rectangles correspond to the small box cuts. Some areas in the parameter space are not covered because they were ruled out by the constraints imposed on the number density.

For each point in the parameter space, we create a galaxy sample out of AbacusSummit simulation. We put a central galaxy in the center of mass of the dark matter halo based on a probability computed with Equation 2. We assign the mean velocity of halo particles to this galaxy. We decide how many satellite galaxies to put in each halo by randomly drawing a number from a Poisson distribution with the mean given by Equation 3. We then randomly pick that many dark matter particles from the halo and assign their position and velocity to the satellites.

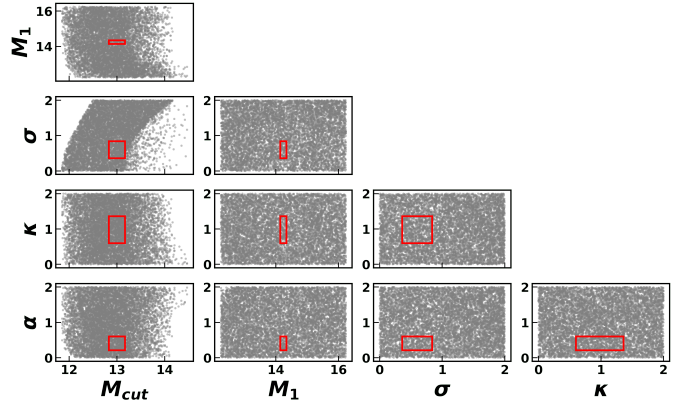


Figure 1: HOD parameter distribution of the full box after filtering. The red boxes show the small box range (see Section 2.3) for the range.

Parameters	Fiducial	Full Box		Small Box	
		Max	Min	Max	Min
$\log M_{\text{cut}}$	13.0	14.5	11.5	13.17	12.83
$\log M_1$	14.24	16.24	12.24	14.33	14.14
σ	0.6	2	0	0.84	0.36
κ	0.98	2	0	1.36	0.59
α	0.4	2	0	0.59	0.2

Table 1: Table for the 5-parameter HOD model. Uniform samples are drawn to populate the HOD model (see Section 2.3).

3. Measurements

For each generated galaxy sample we compute a number of key clustering measures. Each measurement is computed in redshift space by transforming the galaxy coordinates from x, y, z to $x, y, z + v_z(z)/aH(a)$, where we chose the z -direction to be our line of sight, v_z is the z component of the galaxy velocity, a is the scale factor 0.47619, and H is the Hubble parameter $67.36 \text{ km s}^{-1} \text{ Mpc}^{-1}$.

3.1. Projected Two-Point Correlation Function

The main statistics that we use in our tests is the projected two-point correlation function,

$$w_p(r_p) = 2 \int_0^{\pi_{\text{max}}} \xi(r_p, \pi) d\pi. \quad (5)$$

Given a random galaxy, the two-point correlation function $\xi(r_p, \pi)$ is the probability of finding another galaxy within a given distance. This is a function of two variables, projected (r_p) and the line-of-sight (π) separation. The choice of $\pi_{\text{max}} = 60 h^{-1} \text{ Mpc}$ is large enough to include most of the correlated pairs while suppressing the noise from distant uncorrelated pairs, giving a stable result.

We chose 30 logarithmically spaced bins ranging from $r_p = 0.1 h^{-1} \text{ Mpc}$ to $r_p = 31.6 h^{-1} \text{ Mpc}$.

3.2. Void Probability Function

To calculate the void probability function (VPF), we randomly place N_{sphere} number of spheres of radius r in the sim-

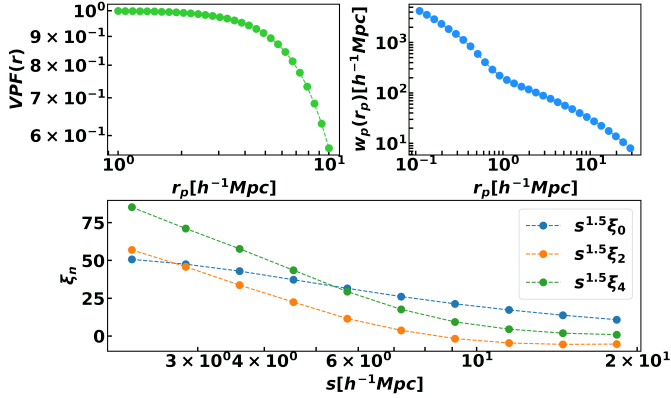


Figure 2: Small scale clustering measurements at the fiducial value from fitting the HOD model at $z = 1.1$. Left top: Void probability function as a function of r ; Right top: projected correlation function as a function of r_p ; Bottom: correlation function as a function of s

ulation box and count the number of void spheres or the number of spheres containing no galaxy (N_{void}). The ratio of the void spheres and the total number of spheres is called the void probability function. VPF is given as

$$VPF(r) = \frac{N_{\text{void}}(r)}{N_{\text{sphere}}(r)}. \quad (6)$$

We used $N_{\text{sphere}} = 10^5$. To compute $VPF(r)$, we chose 30 logarithmically-spaced radii from $r = 1h^{-1}$ Mpc to $r = 10h^{-1}$ Mpc. We use `Halotools`² (v0.7) (Hearin et al., 2017) to compute VPF and w_p .

3.3. Three-Dimensional Redshift-Space Two-Point Correlation Function

We compute the auto-correlation function using the Landy–Szalay estimator (Landy and Szalay, 1993) given by

$$\xi(s, \mu) = \frac{DD(s, \mu) - 2DR(s, \mu) + RR(s, \mu)}{RR(s, \mu)}, \quad (7)$$

where DD , DR , and RR are galaxy-galaxy, galaxy-random and random-random pair count as a function of the bin of separation vector in 3-dimensional space. Where DD is the galaxy-galaxy pair count with certain redshift-space separation s , and cosine of the angle of the pair to the line-of-sight μ . DR is the galaxy-random pair counts and RR is the random-random pair counts.

We then integrate over μ to obtain the angular multipoles of the correlation function

$$\xi_\ell(s) = \frac{2\ell + 1}{2} \int_{-1}^1 \xi(s, \mu) \mathcal{L}_\ell(\mu) d\mu, \quad (8)$$

where $\mathcal{L}_\ell(\mu)$ is the Legendre polynomial of order ℓ . We measure correlation function monopole $\xi_0(s)$, quadrupole ξ_2 and hexadecapole ξ_4 . We chose 10 bins equally spaced in s between $2h^{-1}$ Mpc and $20h^{-1}$ Mpc with $\mu = 100$ (see Fig. 2).

We use `Corrfunc`³ (Sinha and Garrison, 2020; Sinha and Garrison, 2020) for the calculation of ξ_ℓ .

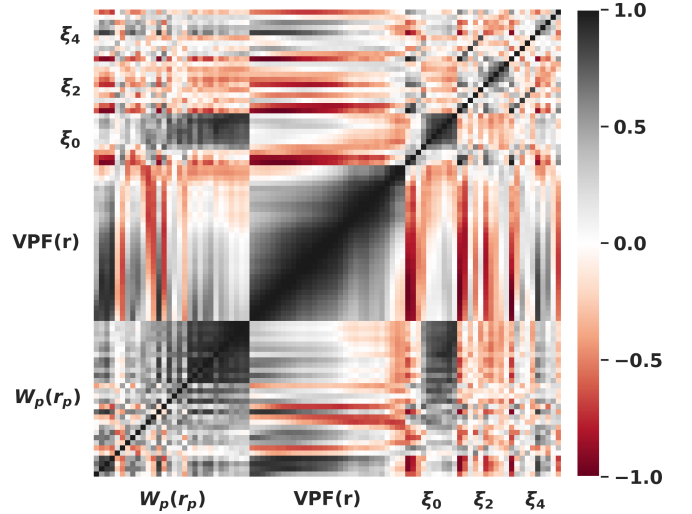


Figure 3: Jackknife Covariance calculated at the fiducial value: from left to right 0-30 $w_p(r_p)$, 30-60 $VPF(r)$, 60-70 ξ_0 , 70-80 ξ_2 , and 80-90 ξ_4

4. Covariance

We use the jackknife resampling technique (Meng Loh, 2008; Norberg et al., 2009; Friedrich et al., 2016; Favole et al., 2021; Mohammad and Percival, 2022) to estimate the covariance matrix of our measurements. The simulation box is divided into 300 overlapping sub-volumes by partitioning it along the x , y , and z axes in three different configurations. First, we create cuboidal sub-volumes with dimensions of $200h^{-1}$ Mpc along the x and y axes and $2000h^{-1}$ Mpc along the z -axis. We then repeat the process by alternating the longer $2000h^{-1}$ Mpc axis between y and z , ensuring that each configuration maintains the same $200h^{-1}$ Mpc dimensions along two axes and $2000h^{-1}$ Mpc along the third axis. This approach results in 300 overlapping cuboidal sub-volumes. We compute the clustering measurements described in Section 3, each time excluding one sub-volume, generating 300 jackknife realizations.

We arrange them in the following order: The w_p measurements followed by VPF , ξ_0 , ξ_2 , and ξ_4 . All the measurements are arranged from the smallest scales to the largest. The jackknife estimate of the covariance matrix is then computed using the formula

$$C_{ij} = \frac{1}{300} \sum_{k,\ell=1}^{300} (X_i^k - \bar{X}_i)(X_j^\ell - \bar{X}_j), \quad (9)$$

$$\bar{X}_i = \frac{1}{300} \sum_{k=1}^{300} X_i^k, \quad (10)$$

where X_i^k denotes the i^{th} element of the measurement vector computed from the k^{th} jackknife realization.

The reduced covariance matrix, defined as

$$R_{ij} = \frac{C_{ij}}{\sqrt{C_{ii}C_{jj}}}, \quad (11)$$

is shown in Fig. 3. The w_p and VPF measurements between neighboring bins are strongly correlated. So are the ξ_ℓ mea-

²<https://halotools.readthedocs.io/en/latest/>

³<https://corrfunc.readthedocs.io/en/master/>

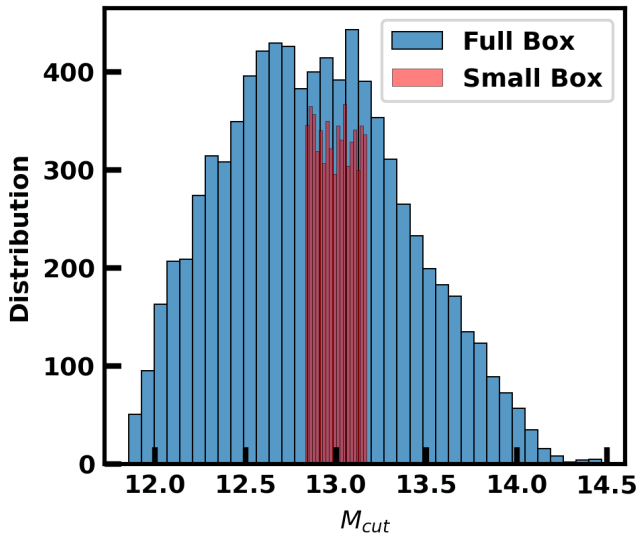


Figure 4: M_{cut} distribution on full and small boxes (see Section 2.3). HOD parameters are drawn uniformly for both the full box and small box and after applying filtering on the full box the distribution is nearly Gaussian.

measurements with different ℓ but similar separation. VPF is not correlated with other clustering measures. These results are in line with theoretical expectations.

These covariance matrices would not be reliable for a robust cosmological analysis. Our goal however is to study the convergence properties of the machine learning-based interpolation methods, and for our purposes, any reasonable positive-definite matrix that loosely resembles a typical covariance matrix of clustering measurements is sufficient to demonstrate the point.

5. Machine Learning Methods

We used supervised ML regression for our work. A more detailed discussion on ML methods is done in Appendix A. Our goal is to be able to predict the measures of small-scale clustering as functions of HOD parameters. Our feature columns are the 5 HOD parameters and our target columns are the w_p , VPF, and ξ_ℓ at different scales. We go through the following sequence of steps:

1. Check the distribution of the data.
2. Data preprocessing.
3. Split the data into train and test.
4. Fit different ML models to train the data.
5. Hyperparameter tuning.
6. Perform accuracy test.
7. Get the best model.

5.1. Check the Distribution of the Data

The distribution of the HOD parameters on both the full and small boxes is drawn from uniform samples. However, due to the filtering method applied on the full box, the M_{cut} parameter has a near Gaussian distribution, as shown in Fig. 4. We suspect some of the inconsistencies in the full box may arise due to this filtering (see Section 6.4).

Statistics	w_p	VPF	ξ_0	ξ_2	ξ_4
lambda_init	0.01	0.1	0.1	0.1	0.1

Table 2: Hyperparameters of Bayesian Ridge regressor for the small box. Only lambda_init is changed during model training keeping other hyperparameters as default.

5.2. Data Preprocessing

We used Scikit-Learn⁴ (Pedregosa et al., 2011) for all the ML-related calculations. To improve the model’s performance, we increased the number of input features by using the *PolynomialFeatures* module followed by the *StandardScaler* module from Scikit-Learn. For the small box, we choose `PolynomialFeatures(degree=2, interaction_only=True)`, resulting in a total of 16 input features for the small box (Discussed in Appendix B). The purpose of using *StandardScaler* is to center the data by subtracting the mean and scaling it to have a unit variance. This preprocessing step is crucial for standardizing the features and ensuring that they contribute equally to the learning process, especially when features have different scales or variances.

The target column, representing the small-scale clustering statistics, is highly skewed which can introduce bias in model training. To avoid this issue, we applied several common data transformation methods, including Log transformation (LT), *StandardScaler* (SC), Yeo-Johnson (YJ), and Box-Cox (BC) to the raw data. These transformations were used to reduce biases, and their importance is further discussed in Section 6.1.

5.3. Split the Data into Train and Test

The data is split into two sets, the training set and the test set, with the latter typically representing 20% of the total data. We train the model using the training set and evaluate its accuracy on the test set. In our study, we used a training set of 6660 and a test set of 1666 for the full box. For the small box, we varied the sample size to investigate its effect on the model’s performance (as shown in Section 6.3), with training set sizes of 800, 1600, and 5400 and a test set size of 600.

5.4. Fit Different ML Models to Train the Data

For better accuracy and robustness, we evaluated several regression models in this study. We tested the performance of three models, namely RF regression, BR regression, and ANN. Each method is discussed in detail in Appendix A.

We found out that ANN works the best among the three methods. A more detailed comparison is discussed in Section 6.2

5.5. Hyperparameter Tuning

Hyperparameter tuning is a crucial step in machine learning, as it helps adjust a model to prevent overfitting or underfitting.

⁴<https://scikit-learn.org/stable/index.html>

Statistics	w_p	VPF	ξ_0	ξ_2	ξ_4
hidden_layer_sizes	500	500	500	500	500
alpha	0.01	0.01	0.01	0.01	0.01
activation	tanh	tanh	tanh	tanh	tanh
learning_rate_init	5×10^{-4}	5×10^{-4}	5×10^{-4}	5×10^{-4}	5×10^{-4}
learning_rate	constant	constant	constant	constant	constant
solver	adam	adam	adam	adam	adam
random_state	1	1	1	1	1
validation_fraction	0.1	0.1	0.2	0.2	0.2
early_stopping	True	True	True	True	True
max_iter	2000	5000	2000	2000	2000

Table 3: Hyperparameters of ANN for the small box.

We used the Scikit-Learn library to perform the following hyperparameter tuning for three models.

For the small box dataset, we used the BayesianRidge module for the BR model. The modified hyperparameters are shown in Table 2, while all other parameters were kept at their default values. We used the MLPRegressor module for the ANN model, and the corresponding hyperparameters are listed in Table 3.

We tested the RF model only on w_p using the RandomForestRegressor module with `n_estimators=200`, `criterion='squared_error'`, `bootstrap=False`, `random_state=0`, `warm_start=True`, while keeping all other parameters at their default settings. RF is a widely used method that has been applied to various cosmological problems in previous studies (Lucie-Smith et al., 2018; Nadler et al., 2018; Cohn and Battaglia, 2020; Mucesh et al., 2021). RF is not a good choice for our problem as it relies on a series of decision rules based on individual features, which may not capture the full complexity of the data.

5.6. Perform Accuracy Test

Numerous performance measures are employed to assess the efficacy of an ML model, such as the root mean squared error (RMSE), mean absolute error (MAE), and adjusted R^2 score (see Appendix B). Since each bin in our clustering statistics has a different range, we utilize modified versions of RMSE and MAE namely average percent RMSE and average percent

Model	(%) \overline{RMSE}	(%) \overline{MAE}	Adj $\overline{R^2}$	(%) RMSE Range	(%) MAE Range
RF	2.55	1.57	0.982	4.86 - 1.26	3 - 0.8
BR	1.24	0.94	0.995	1.78 - 0.78	1.29 - 0.65
ANN	0.63	0.48	0.999	1.11 - 0.35	0.72 - 0.27

Table 4: Comparison of RF, BR, ANN regression model performance on w_p for the small box test set. We calculate the average percent RMSE, average percent MAE, and average R^2 score for comparing the model performance (see Section 5.6 for definition).

Model	Bin No.	5 Best (%) RMSE	Bin No.	5 Worst (%) RMSE
RF	30	1.26	1	4.88
	29	1.26	2	4.84
	28	1.28	3	4.78
	27	1.31	4	4.72
	26	1.34	5	4.66
BR	30	0.78	9	1.78
	29	0.8	6	1.78
	28	0.81	7	1.77
	26	0.82	5	1.76
	27	0.84	1	1.73
NN	28	0.35	3	1.11
	29	0.36	5	1.02
	27	0.36	1	1.0
	30	0.38	2	1.0
	25	0.38	4	0.98

Table 5: Performance for 5 best and worst outputs of w_p on Box-Cox transformation for the small box test set. We compare RF, BR, and ANN models to report the percent RMSE.

Adjusted R^2	Small Box			Full Box	
	RF	BR	ANN	BR	ANN
Unscaled	0.966	0.99	0.97	0.885	0.98
Standard Scalar	0.982	0.99	0.998	0.885	0.994
Yeo-Jhonson	0.983	0.995	0.999	-	-
Box-Cox	0.982	0.995	0.999	-	-

Table 6: Adjusted R^2 score of w_p on Box-Cox transformation for the small box test set and full box test set. We compare RF, BR, and ANN models to report the Adjusted R^2 score

MAE respectively. The average percent RMSE is defined as

$$(\%) \overline{RMSE} = \frac{1}{n_{bins}} \sum_{i=1}^{n_{bins}} \frac{RMSE_i}{\left(\frac{|y_{max}^i| + |y_{min}^i|}{2}\right)} \times 100. \quad (12)$$

The average percent MAE is defined as

$$(\%) \overline{MAE} = \frac{1}{n_{bins}} \sum_{i=1}^{n_{bins}} \frac{MAE_i}{\left(\frac{|y_{max}^i| + |y_{min}^i|}{2}\right)} \times 100, \quad (13)$$

where n_{bins} is the number of bins, and for the i_{th} bin, y_{max}^i and y_{min}^i represent the maximum and minimum truth values, respectively. Similarly, the average adjusted R^2 (Adj $\overline{R^2}$) score is calculated by taking the sum of total adjusted R^2 scores and dividing it by n_{bins} . We present results solely for the projected correlation function on the small box. However, we performed the same analysis on other statistics when selecting an optimal model.

In Table 4, we compare $(\%) \overline{RMSE}$, $(\%) \overline{MAE}$, and average adjusted $\overline{R^2}$ score on RF, BR, and ANN. The ANN outperforms RF and BR by a considerable margin. Table 5 displays the best 5 and worst 5 bins for $(\%) \overline{RMSE}$. All models exhibit superior performance at larger projected separations (r_p). The results for the full box and the small box can be found in Table 6. We do not include results for YJ and BC for the full box due to their inconsistency with sparse data. For all models, except BR on the full box, performance scores are acceptable (Adjusted R^2 score is above 0.95 on the test set). Typically, this would be considered a satisfactory performance; however, we will later demonstrate that even with such a high-performance score, the models result in strongly biased posterior likelihood contours.

Furthermore, we examine the cross-validation scores for all statistics to assess the uniformity of the data and conclude that the variance was reduced with data transformation.

5.7. Likelihood Analysis

We perform MCMC (Foreman-Mackey et al., 2013) to obtain the posterior probability distribution of parameter space. The likelihood function $\mathcal{L} \propto \exp(-\chi^2/2)$, where χ^2 is given by

$$\chi^2 = (x - \mu)^T C^{-1} (x - \mu). \quad (14)$$

In our analysis, x denotes the machine learning model predictions (‘theory’), while μ represents the actual simulation measurements (‘observation’). Specifically, we applied this framework to w_p , VPF , and, ξ_ℓ , as well as their combinations (see Section 7). Here, $(x - \mu)$ is the difference between theory and observation and C^{-1} is the inverse of the covariance matrix. We use `Emcee`⁵ to estimate the posterior distribution of the model parameters. Several combinations of statistics were tested using 250 walkers, with the first 200 steps discarded as burn-in. Given the model’s efficiency, we achieved convergence within a minute. Our findings are discussed in detail in the next section.

6. Constraining HOD parameters

The ultimate objective of ML-based emulators is to be able to run MCMC chains on measured data to constrain HOD parameters. While all our approaches yield acceptable performance metrics, we will demonstrate that unless considerable care is exercised, they result in inaccurate likelihood surfaces. The cumulative effect of small inaccuracies significantly biases the best-fit values and often leads to underestimated uncertainties in derived model parameters. This holds true even when we constrain ourselves to the small box where the HOD parameter range is narrow. We will present results for the w_p , but the general conclusions are similar for all other statistics. Despite our model’s ability to accurately predict the full projected correlation function, we only selected $r_p = 1.77h^{-1}$ Mpc to $r_p = 17.78h^{-1}$ Mpc (bin 15 – bin 27) for our MCMC run. This was done to maintain consistency with the ξ_ℓ range ($s = 2h^{-1}$ Mpc – $20h^{-1}$ Mpc), as we will demonstrate how HOD constraints improve with the combination of clustering statistics (see Section 7).

6.1. Effect of Data Transformations

We find that data transformations are essential. Without them, the likelihood contours are strongly biased. Fig. 5 shows the distribution of the inaccuracy in the ANN-based emulator prediction at different HOD parameter values (left panel), and the resulting one and two σ contours in the σ vs $\log M_1$ plane. We compute this for unscaled data and three different data transformation algorithms: SC, BC, and, YJ. The likelihood contours are strongly biased when no transformation is applied. However, applying a data transformation corrects this bias.

Despite the standard scalar transformation exhibiting an off-center error distribution, we find that all three approaches perform equally well when it comes to the likelihood contours. The bias in the computed likelihood function is much larger than what the left panel of Fig. 5 would suggest. The error in the density plots, represented as $Error/\sigma$, is calculated as the difference between the predicted values from the machine learning models and the true values obtained from the simulation, normalized by the standard deviation (σ) derived from the jackknife covariance matrix. Specifically, for each predicted value y_i , the error is computed as $Error_i = y_i^{pred} - y_i^{true}$, where σ_i is the jackknife estimate of the standard deviation for the i^{th} data point. This normalization allows for a clearer interpretation of the prediction errors by accounting for the intrinsic variability in the data. All the Error calculations shown in this work are calculated on w_p . However, we found similar results for the other measurements (VPF , ξ_ℓ) as well.

Fig. 6 shows similar computation for the BR method. The data scaling is essential here as well. Unlike the ANN, however, none of the transformations can produce unbiased likelihood contours, even though the YJ and the BC transformations lead to consistent results. Here as well, the bias in the likelihood contours is much more visible than what the error distribution plot would suggest.

⁵<https://emcee.readthedocs.io/en/stable/>

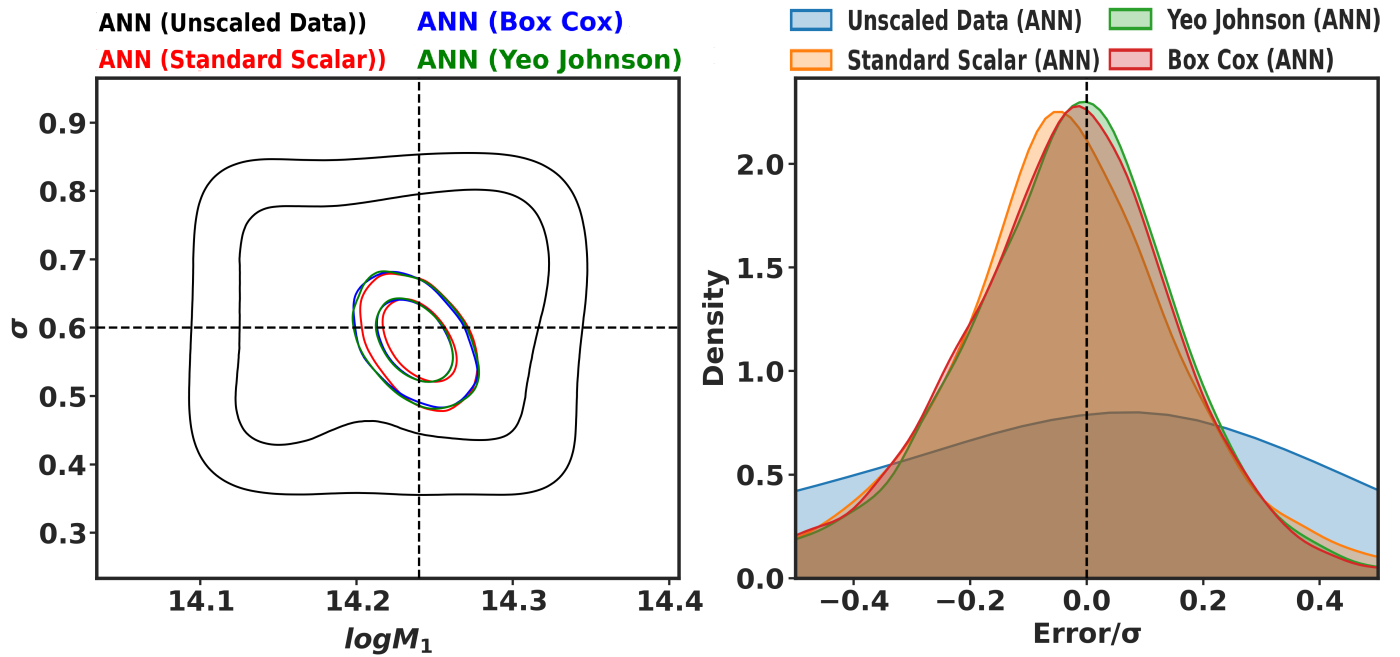


Figure 5: Exploring the impact of data transformation on ANN Method within the small Box. Left: Equipotential contours of the MCMC posterior from fitting the HOD model at $z = 1.1$ using w_p . The plot shows the convergence between transformed and non-transformed data. Right: Density plot between Transformed vs. Non-transformed Data as a function of Error/ σ . The σ is calculated from the jackknife covariance matrix.

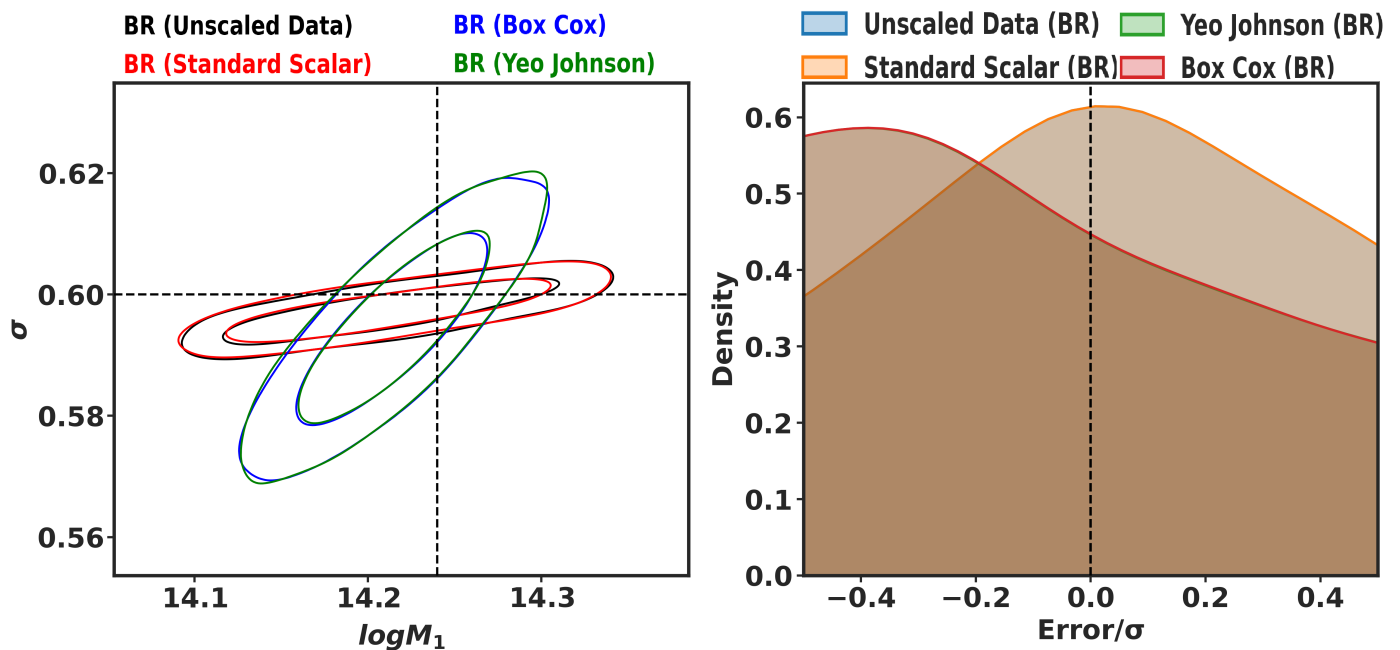


Figure 6: Exploring the impact of data transformation on BR Method within the small Box. Left: Equipotential contours of the MCMC posterior from fitting the HOD model at $z = 1.1$ using w_p . The plot shows the convergence between transformed and non-transformed data. Right: Density plot between Transformed vs. Non-transformed Data as a function of Error/ σ . The σ is calculated from the jackknife covariance matrix.

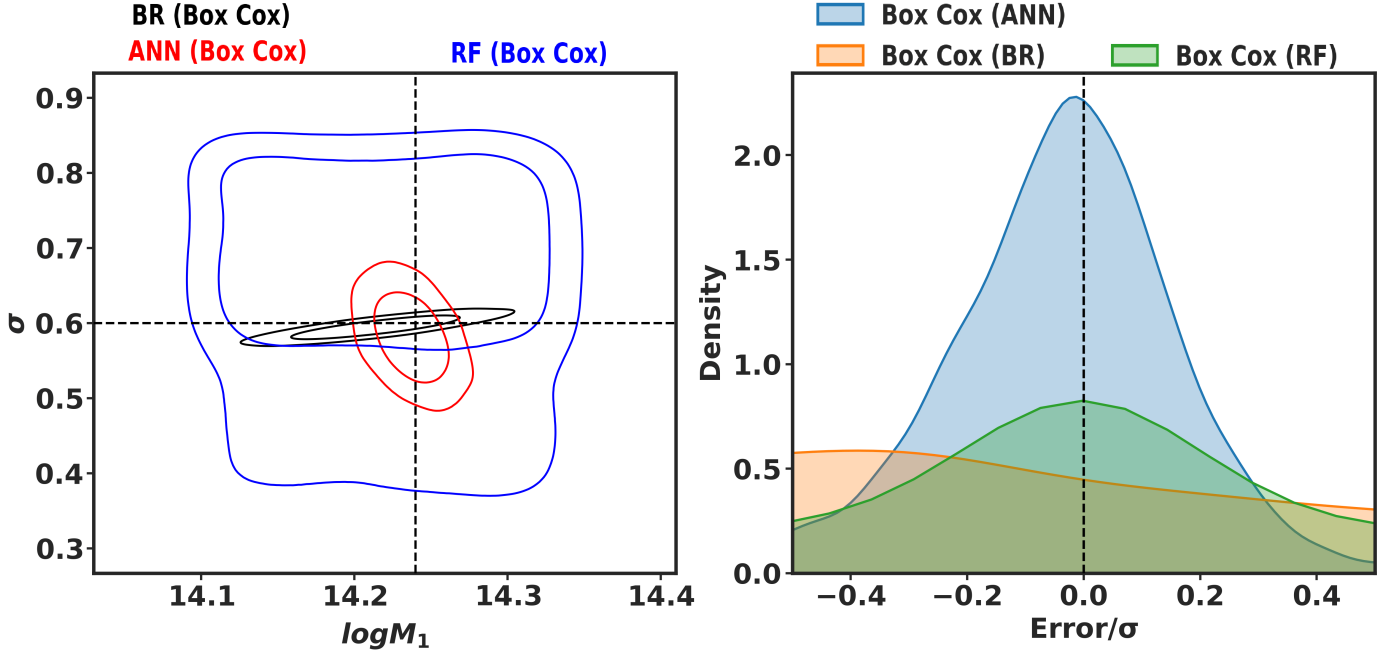


Figure 7: Exploring the impact of different ML methods within the small box. Left: Equipotential contours of the MCMC posterior from fitting the HOD model at $z = 1.1$ using w_p . The plot shows the convergence test between the RF, BR, and ANN models. Right: Density plot between the RF, BR, and ANN models as a function of Error/σ . The σ is calculated from the jackknife covariance matrix.

6.2. Algorithm Choice

Fig. 7 shows the error distribution and the HOD parameter likelihood contours for all three ML algorithms considered in this work. In all three cases, the BC transformation was applied to the data. The right panel on Fig. 7 shows that the ANN-based method is the least biased. The BR and RF methods result in significantly wider likelihood contours compared to the ANN, which is the one closest to the truth. In the case of RF, the likelihood contours are completely dominated by the prior parameters.

6.3. Number of Samples

We anticipate that all methods will eventually converge towards the truth as the size of the training sample increases. On the other hand, an excessively large training sample would defeat the primary purpose of the emulator, which is to obtain likelihoods with significantly less computational time.

Fig. 8 shows the effect of increasing sample size on our results for the BR method. We see that increasing the sample size by a factor of two and then a factor of seven does not have a significant effect on the performance of the algorithm.

For the ANN algorithm, on the other hand, the improvement in the size of the training data is clearly visible. The four panels in Fig. 9 shows the evolution of the error distribution as the sample size first doubles and then increases by a factor of seven. The improvement in this distribution, however, is not as drastic as one would hope.

These findings suggest that for the BR method, increasing the sample size does not yield significant improvement, while for ANN, increasing the sample size can improve performance.

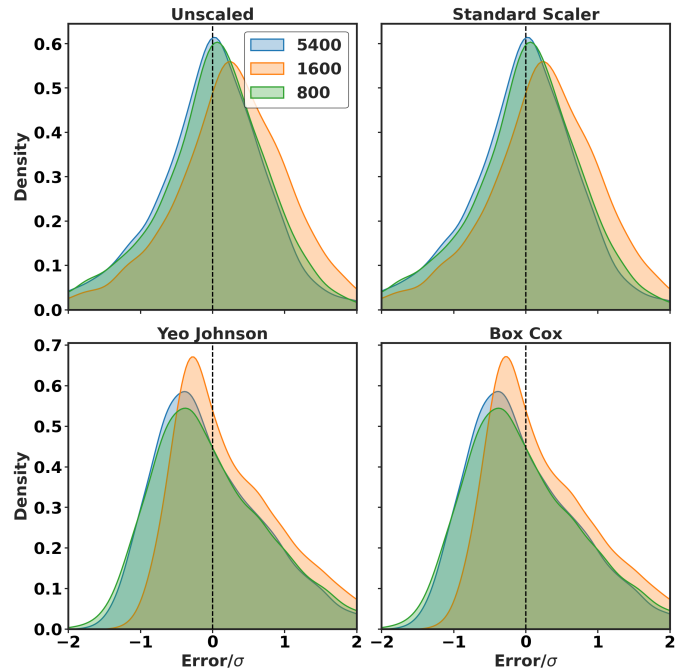


Figure 8: Effect of increasing data points on Bayesian Ridge Regressor for the small box. This plot compares the density plot between the training set of 800, 1600, and 5400 for unscaled, SC, YJ, and BC transformation as a function of Error/σ . The σ is calculated from the jackknife covariance matrix.

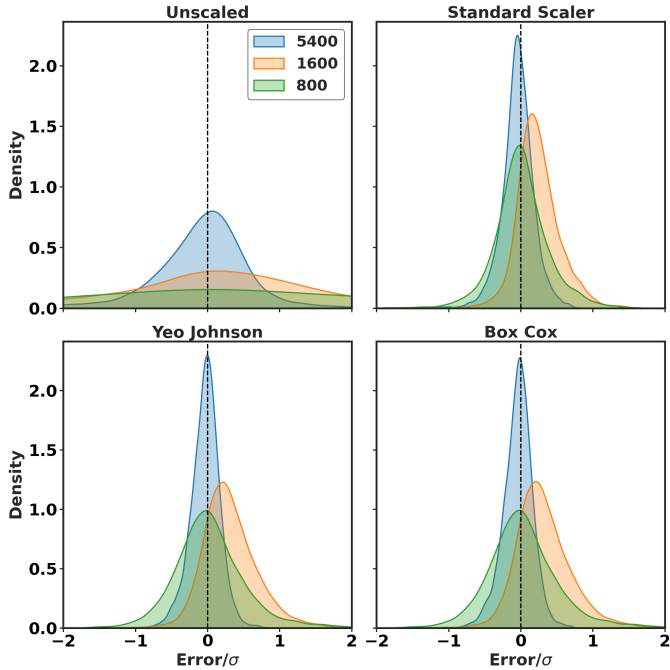


Figure 9: Effect of increasing data points on ANN for the small box. This plot compares the density plot between the training set of 800, 1600, and 5400 for unscaled, SC, YJ, and BC transformation as a function of Error/σ . The σ is calculated from the jackknife covariance matrix.

6.4. Prior Parameter Ranges

Fig. 10 shows the effect of increasing the prior range of HOD parameter space that the ML algorithm has to deal with. The black and red contours on the left panel correspond to the small box and full box respectively as defined in Section 2. The contours were derived with the ANN algorithm using the BC data transformation for the small box and SC for the full box, the method that was performing the best on a smaller box as described in Section 6.2. From Fig. 10 it is clear that even the best-performing algorithm fails to accurately reproduce the likelihood surfaces when the parameter range gets too large. In the limit of a very large number of training samples, we still expect the ANN to reproduce the true likelihood faithfully. This would, however, require a very large training sample and the computational cost of training the network will start approaching that of a straightforward MCMC chain.

7. Results and Conclusions

Small-scale clustering of galaxies potentially contains useful information about cosmological parameters. To harness this information, however, one needs to first accurately model the nonlinear process of galaxy formation. For clustering measurements relevant to cosmology, the most important aspect is determining which types of galaxies occupy dark matter halos and exactly how they are distributed within those halos. The HOD-based family of models is one of the most widely used methods for modeling this galaxy-halo connection. Since generating HOD model predictions requires computationally ex-

pensive computations from N-body simulations, ML-based approaches that can significantly accelerate this computation have been used very frequently recently.

We found that great care must be taken when modeling the dependence of small-scale clustering on HOD parameters. Transforming the input data, the choice of the ML approach, and the size of the HOD space under exploration, have a big impact on the robustness of the predictions. We found that very often the ML methods report acceptable formal performance scores, but when the inaccuracies in the ML modeling are propagated to the quantities that are actually important for cosmology, these small inaccuracies lead to unacceptable large biases. For example, the posterior likelihood in the HOD space can be strongly biased even when the ML pipeline reports a good performance score.

For the galaxy tracers and clustering measurements we used, we found that artificial neural networks (ANN) provided the best results among the models tested. Even for the ANN, the results were robust only when the HOD space was confined to the small box with a relatively narrow range of the parameters allowed and failed when we looked at larger parameter spaces. The selection of the small box range is largely driven by M_{cut} , as this parameter is particularly sensitive to the filtering method we employed. In contrast, the other HOD parameters could potentially span larger ranges, as their distributions are less affected by this filtering process. The required restriction on the HOD parameter space was significant, being much smaller than the typical HOD parameter bounds allowed by currently available data. The ANN results become more robust with a larger set of training data as expected, but we found that the convergence to the true result with the training data size is not as fast as one would hope. The other two ML-based methods that we tried were the Bayesian Ridge and the Random Forest. These methods resulted in very large biases in the likelihood values even for the small box restriction.

Once the ML models achieve the desired robustness, the constraints on HOD parameters can be obtained with very little computational time. We checked how different combinations of w_p , VPF , and ξ_ℓ enhanced the constraining power of small-scale clustering on the HOD parameter space. The results of this exercise are shown in Table 7 and the 1σ posterior contours are shown in Fig. 11. The improvement in the HOD parameter constraints is shown in Fig. 12. We find that the addition of VPF to w_p resulted in a slight improvement, but the combination of $w_p + \xi_0$ worked better than $w_p + VPF$. These results are qualitatively in agreement with previous findings but want to warn the reader to treat the actual numbers (error bars, etc.) with caution. They should not be interpreted as actual forecasts for this type of analysis. The actual errors are very likely underestimated due to the usage of Jackknife covariance matrices and the prior effects from the small box restriction of allowable HOD space.

Acknowledgements

This work is supported by DOE grants DE-SC0021165 and DE-SC0011840.

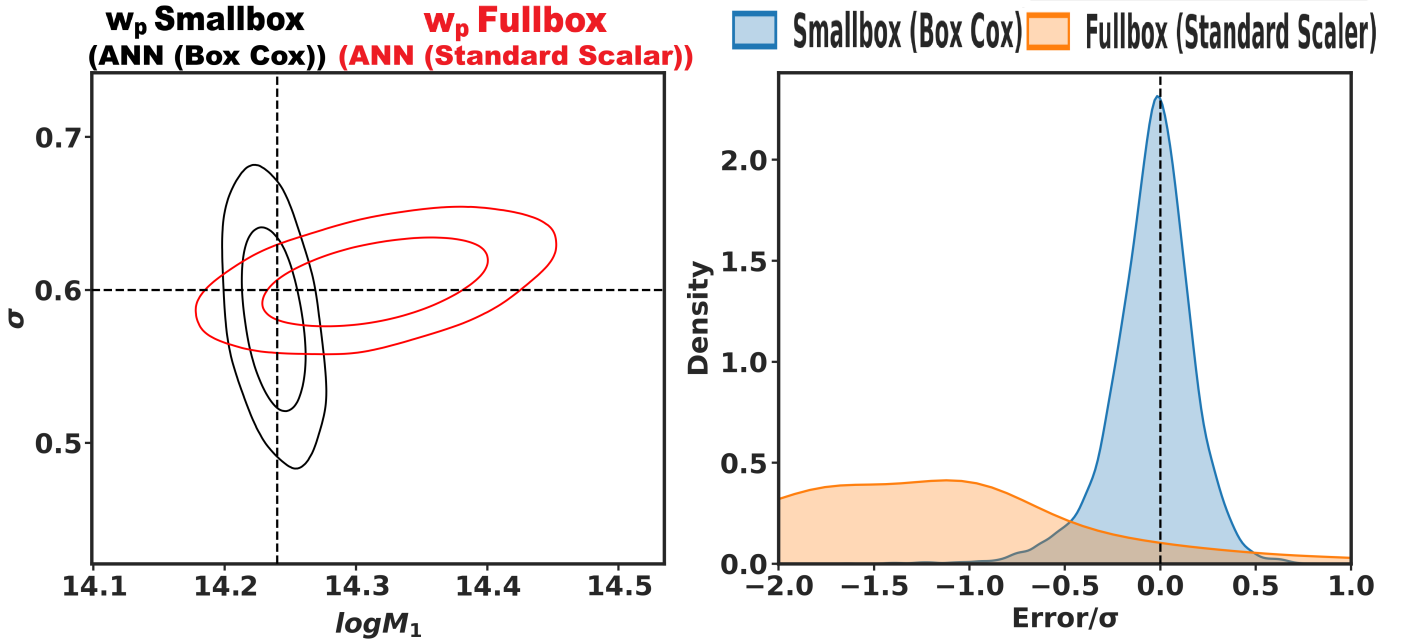


Figure 10: Error Comparison Between full Box and small box. Left: Equipotential contours of the MCMC posterior from fitting the HOD model at $z = 1.1$ using w_p . This plot shows the convergence between different box sizes. Right: Density plot between small box and full box as a function of Error/σ . The σ is calculated from the jackknife covariance matrix.

Observables	1 σ error				
	Small Box				
	$\log M_{\text{cut}}$	$\log M_1$	σ	κ	α
w_p	$12.9988^{+0.011}_{-0.0111}$	$14.2414^{+0.0099}_{-0.0103}$	$0.5955^{+0.0136}_{-0.0138}$	$0.9859^{+0.023}_{-0.0226}$	$0.4005^{+0.0101}_{-0.0106}$
$w_p + VPF$	$12.9989^{+0.0103}_{-0.011}$	$14.2409^{+0.0097}_{-0.0096}$	$0.5962^{+0.0125}_{-0.013}$	$0.9856^{+0.0206}_{-0.0214}$	$0.4001^{+0.0088}_{-0.0091}$
$w_p + \xi_0$	$12.9984^{+0.0069}_{-0.007}$	$14.2416^{+0.008}_{-0.008}$	$0.5954^{+0.0121}_{-0.0121}$	$0.9848^{+0.0194}_{-0.0191}$	$0.4007^{+0.0089}_{-0.0086}$
$w_p + \xi_0 + \xi_2$	$12.9988^{+0.0064}_{-0.0066}$	$14.2416^{+0.0075}_{-0.0073}$	$0.5956^{+0.0116}_{-0.0117}$	$0.985^{+0.0182}_{-0.0185}$	$0.4001^{+0.0085}_{-0.0085}$
$w_p + \xi_0 + \xi_2 + \xi_4$	$12.9983^{+0.0058}_{-0.0059}$	$14.2411^{+0.0069}_{-0.0073}$	$0.5953^{+0.0113}_{-0.0113}$	$0.9841^{+0.0179}_{-0.0178}$	$0.3998^{+0.0081}_{-0.0081}$
ξ_0	$12.9975^{+0.0132}_{-0.0135}$	$14.2426^{+0.0113}_{-0.0113}$	$0.5941^{+0.0326}_{-0.0337}$	$0.9825^{+0.0583}_{-0.0558}$	$0.4005^{+0.0267}_{-0.0262}$
$\xi_0 + \xi_2$	$12.9986^{+0.0117}_{-0.0122}$	$14.2418^{+0.0101}_{-0.0099}$	$0.5965^{+0.0276}_{-0.0263}$	$0.9769^{+0.0508}_{-0.051}$	$0.3984^{+0.0224}_{-0.0222}$
$\xi_0 + \xi_2 + \xi_4$	$12.9986^{+0.0111}_{-0.0113}$	$14.2419^{+0.009}_{-0.0096}$	$0.5984^{+0.0267}_{-0.0273}$	$0.9707^{+0.0433}_{-0.0424}$	$0.396^{+0.0177}_{-0.0178}$
$w_p + VPF + \xi_0 + \xi_2 + \xi_4$	$12.9984^{+0.0056}_{-0.0056}$	$14.2409^{+0.0067}_{-0.0068}$	$0.596^{+0.0104}_{-0.0105}$	$0.9826^{+0.0158}_{-0.0166}$	$0.3999^{+0.0072}_{-0.0074}$

Table 7: 1 σ error for the small box. The values are calculated by running the MCMC chain and using the ANN models for w_p , VPF, ξ_0 , ξ_2 , and ξ_4 .

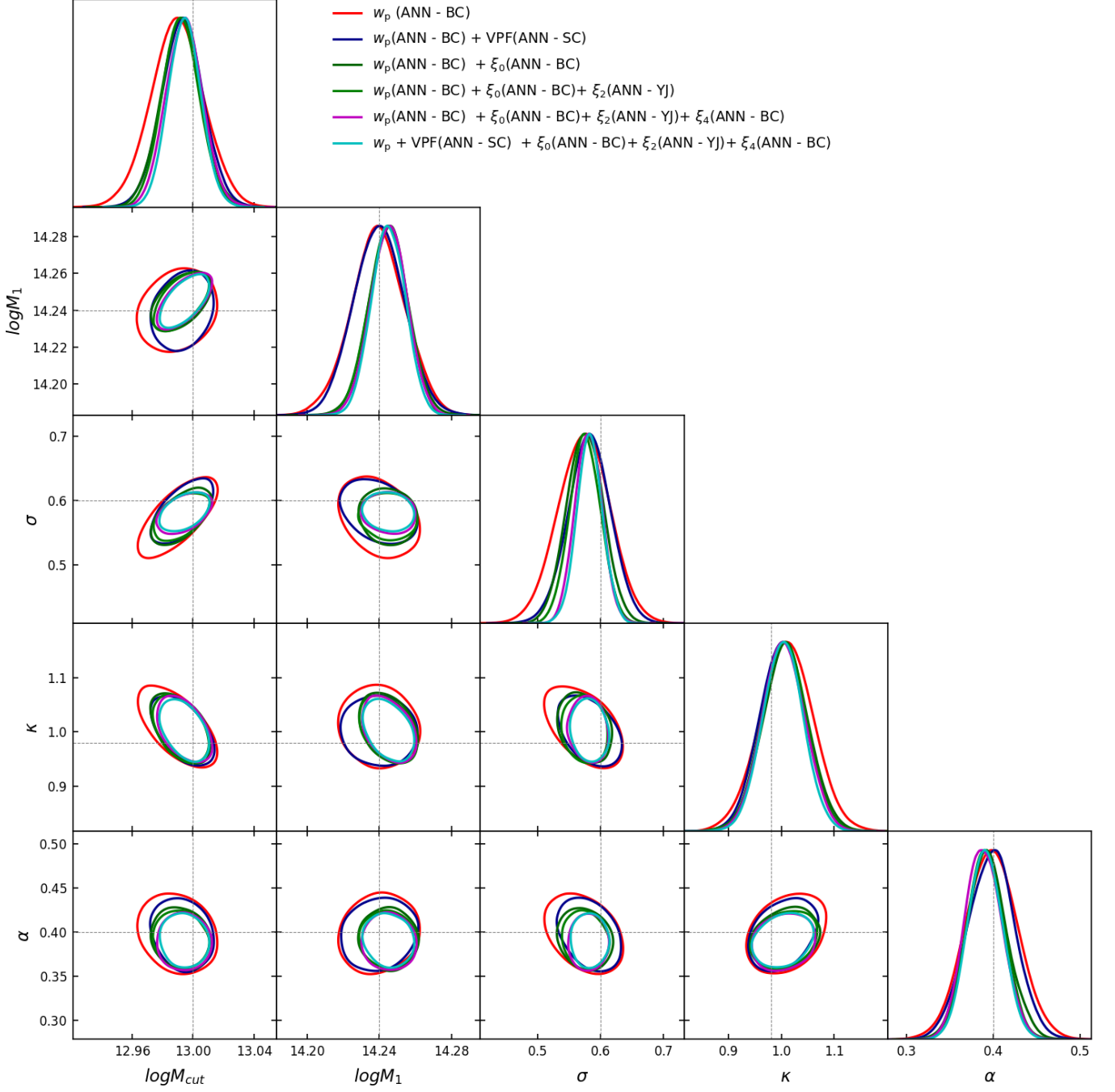


Figure 11: Equipotential contours of the MCMC posterior from fitting the HOD model at $z = 1.1$. The ANN models are trained on the small box for w_p , VPF, ξ_0 , ξ_2 , and ξ_4 . The dashed lines denote the expected values of the HOD parameters. Contours are generated using the best-performing combinations of the ML models.

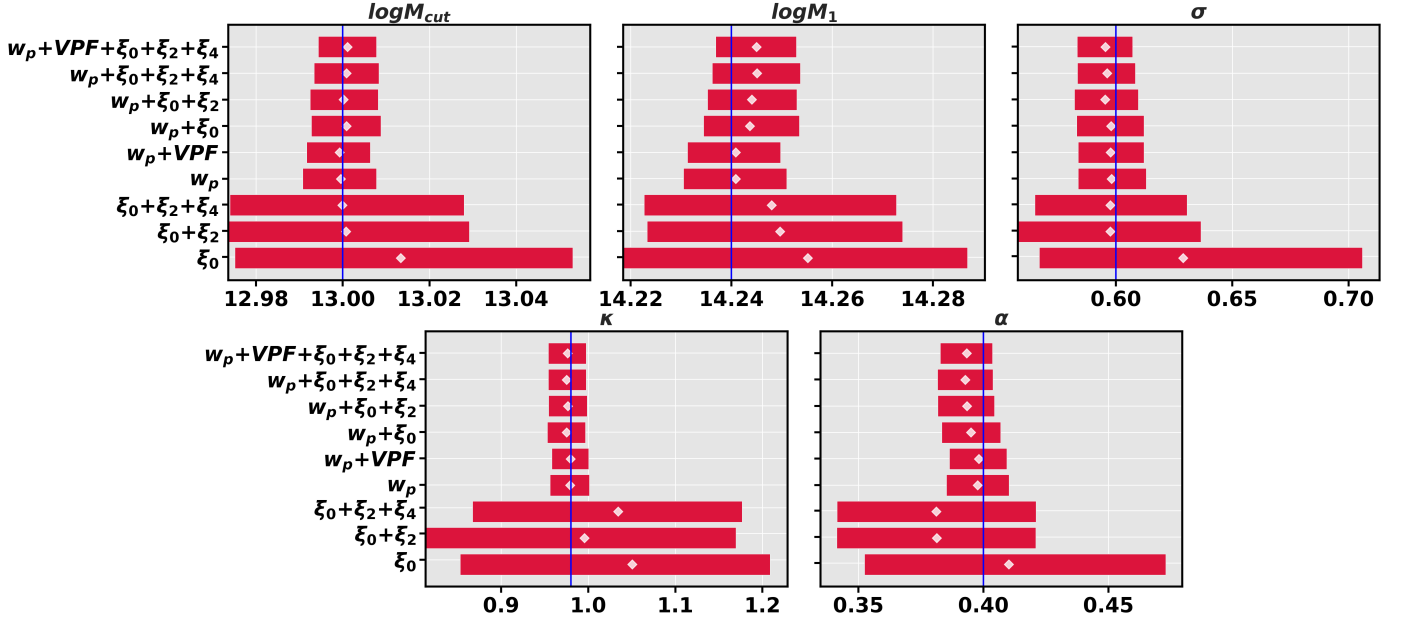


Figure 12: Effect of 1σ constraint on HOD parameters for a different combination of statistics. The blue lines denote the expected values of the HOD parameters. The white marks at the center of the red bars represent the mean of the MCMC samples after discarding 200 steps as burn-in.

This research used resources from the National Energy Research Scientific Computing Center (NERSC), a U.S. Department of Energy Office of Science User Facility located at Lawrence Berkeley National Laboratory, operated under Contract No. DE-AC02-05CH11231.

AJ thanks Andrew Hearin and Hanyu Zhang for useful discussions and comments.

Data Availability

The data products related to this study will be shared upon request. The AbacusSummit simulations are publicly available to download from <https://abacusnbody.org/>.

References

Agarwal, S., Davé, R., Bassett, B.A., 2018. Painting galaxies into dark matter haloes using machine learning. *MNRAS* 478, 3410–3422. doi:[10.1093/mnras/sty1169](https://doi.org/10.1093/mnras/sty1169), [arXiv:1712.03255](https://arxiv.org/abs/1712.03255).

Alam, S., Peacock, J.A., Kraljic, K., Ross, A.J., Comparat, J., 2020. Multi-tracer extension of the halo model: probing quenching and conformity in eBOSS. *Mon. Not. Roy. Astron. Soc.* 497, 581–595. doi:[10.1093/mnras/staa1956](https://doi.org/10.1093/mnras/staa1956), [arXiv:1910.05095](https://arxiv.org/abs/1910.05095).

Alfaro, I.G., Rodriguez, F., Ruiz, A.N., Lambas, D.G., 2020. How galaxies populate haloes in very low-density environments. An analysis of the halo occupation distribution in cosmic voids. *A&A* 638, A60. doi:[10.1051/0004-6361/201937431](https://doi.org/10.1051/0004-6361/201937431), [arXiv:2003.06255](https://arxiv.org/abs/2003.06255).

Alfaro, I.G., Rodriguez, F., Ruiz, A.N., Luparello, H.E., Lambas, D.G., 2022. How galaxies populate halos in extreme density environments: An analysis of the halo occupation distribution in SDSS. *A&A* 665, A44. doi:[10.1051/0004-6361/202243542](https://doi.org/10.1051/0004-6361/202243542), [arXiv:2203.07526](https://arxiv.org/abs/2203.07526).

Alfaro, I.G., Ruiz, A.N., Luparello, H.E., Rodriguez, F., Garcia Lambas, D., 2021. Galaxy populations in haloes in high-density environments. *A&A* 654, A62. doi:[10.1051/0004-6361/202039838](https://doi.org/10.1051/0004-6361/202039838), [arXiv:2106.08989](https://arxiv.org/abs/2106.08989).

Angulo, R.E., Springel, V., White, S.D.M., Jenkins, A., Baugh, C.M., Frenk, C.S., 2012. Scaling relations for galaxy clusters in the Millennium-XXL

simulation. *MNRAS* 426, 2046–2062. doi:[10.1111/j.1365-2966.2012.21830.x](https://doi.org/10.1111/j.1365-2966.2012.21830.x), [arXiv:1203.3216](https://arxiv.org/abs/1203.3216).

Artale, M.C., Zehavi, I., Contreras, S., Norberg, P., 2018. The impact of assembly bias on the halo occupation in hydrodynamical simulations. *MNRAS* 480, 3978–3992. doi:[10.1093/mnras/sty2110](https://doi.org/10.1093/mnras/sty2110), [arXiv:1805.06938](https://arxiv.org/abs/1805.06938).

Bédorf, J., Gaburov, E., Portegies Zwart, S., 2012. Bonsai: A GPU Tree-Code, in: Capuzzo-Dolcetta, R., Limongi, M., Tornambè, A. (Eds.), *Advances in Computational Astrophysics: Methods, Tools, and Outcome*, p. 325. doi:[10.48550/arXiv.1204.2280](https://doi.org/10.48550/arXiv.1204.2280), [arXiv:1204.2280](https://arxiv.org/abs/1204.2280).

Berlind, A.A., Weinberg, D.H., 2002. The Halo Occupation Distribution: Toward an Empirical Determination of the Relation between Galaxies and Mass. *ApJ* 575, 587–616. doi:[10.1086/341469](https://doi.org/10.1086/341469), [arXiv:astro-ph/0109001](https://arxiv.org/abs/astro-ph/0109001).

Biau, G., Scornet, E., 2015. A Random Forest Guided Tour. *arXiv e-prints*, [arXiv:1511.05741](https://arxiv.org/abs/1511.05741)doi:[10.48550/arXiv.1511.05741](https://doi.org/10.48550/arXiv.1511.05741), [arXiv:1511.05741](https://arxiv.org/abs/1511.05741).

Bose, S., Eisenstein, D.J., Hernquist, L., Pillepich, A., Nelson, D., Marinacci, F., Springel, V., Vogelsberger, M., 2019. Revealing the galaxy-halo connection in IllustrisTNG. *MNRAS* 490, 5693–5711. doi:[10.1093/mnras/stz2546](https://doi.org/10.1093/mnras/stz2546), [arXiv:1905.08799](https://arxiv.org/abs/1905.08799).

Breiman, L., 2001. Random Forests. *Machine Learning* 45, 5–32. doi:[10.1023/A:1010933404324](https://doi.org/10.1023/A:1010933404324).

Chai, T., Draxler, R.R., 2014. Root mean square error (rmse) or mean absolute error (mae)? – arguments against avoiding rmse in the literature. *Geoscientific Model Development* 7, 1247–1250. URL: <https://gmd.copernicus.org/articles/7/1247/2014/>, doi:[10.5194/gmd-7-1247-2014](https://doi.org/10.5194/gmd-7-1247-2014).

Cohn, J.D., Battaglia, N., 2020. Multiwavelength cluster mass estimates and machine learning. *MNRAS* 491, 1575–1584. doi:[10.1093/mnras/stz3087](https://doi.org/10.1093/mnras/stz3087), [arXiv:1905.09920](https://arxiv.org/abs/1905.09920).

Cooray, A., Sheth, R., 2002. Halo models of large scale structure. *Phys. Rep.* 372, 1–129. doi:[10.1016/S0370-1573\(02\)00276-4](https://doi.org/10.1016/S0370-1573(02)00276-4), [arXiv:astro-ph/0206508](https://arxiv.org/abs/astro-ph/0206508).

Davé, R., Anglés-Alcázar, D., Narayanan, D., Li, Q., Rafieferantsoa, M.H., Appleby, S., 2019. SIMBA: Cosmological simulations with black hole growth and feedback. *MNRAS* 486, 2827–2849. doi:[10.1093/mnras/stz937](https://doi.org/10.1093/mnras/stz937), [arXiv:1901.10203](https://arxiv.org/abs/1901.10203).

Dawson, K.S., Schlegel, D.J., Ahn, C.P., Anderson, S.F., Aubourg, É., Bailey, S., Barkhouser, R.H., Bautista, J.E., Beifiori, A., Berlind, A.A., Bhardwaj, V., Bizyaev, D., Blake, C.H., Blanton, M.R., Blomqvist, M., Bolton, A.S., Borde, A., Bovy, J., Brandt, W.N., Brewington, H., Brinkmann, J., Brown,

- P.J., Brownstein, J.R., Bundy, K., Busca, N.G., Carithers, W., Carnero, A.R., Carr, M.A., Chen, Y., Comparat, J., Connolly, N., Cope, F., Croft, R.A.C., Cuesta, A.J., da Costa, L.N., Davenport, J.R.A., Delubac, T., de Putter, R., Dhital, S., Ealet, A., Ebelke, G.L., Eisenstein, D.J., Escoffier, S., Fan, X., Filiz Ak, N., Finley, H., Font-Ribera, A., Génova-Santos, R., Gunn, J.E., Guo, H., Haggard, D., Hall, P.B., Hamilton, J.C., Harris, B., Harris, D.W., Ho, S., Hogg, D.W., Holder, D., Honscheid, K., Huehnerhoff, J., Jordan, B., Jordan, W.P., Kauffmann, G., Kazin, E.A., Kirkby, D., Klaene, M.A., Kneib, J.P., Le Goff, J.M., Lee, K.G., Long, D.C., Loomis, C.P., Lundgren, B., Lupton, R.H., Maia, M.A.G., Makler, M., Malanushenko, E., Malanushenko, V., Mandelbaum, R., Manera, M., Maraston, C., Margala, D., Masters, K.L., McBride, C.K., McDonald, P., McGreer, I.D., McMahon, R.G., Mena, O., Miralda-Escudé, J., Montero-Dorta, A.D., Montesano, F., Muna, D., Myers, A.D., Naugle, T., Nichol, R.C., Noterdaeme, P., Nuza, S.E., Olmstead, M.D., Oravetz, A., Oravetz, D.J., Owen, R., Padmanabhan, N., Palanque-Delabrouille, N., Pan, K., Parejko, J.K., Pâris, I., Percival, W.J., Pérez-Fournon, I., Pérez-Ràfols, I., Petitjean, P., Pfaffenberger, R., Pforr, J., Pieri, M.M., Prada, F., Price-Whelan, A.M., Raddick, M.J., Rebolo, R., Rich, J., Richards, G.T., Rockosi, C.M., Roe, N.A., Ross, A.J., Ross, N.P., Rossi, G., Rubiño-Martín, J.A., Samushia, L., Sánchez, A.G., Sayres, C., Schmidt, S.J., Schneider, D.P., Scóccola, C.G., Seo, H.J., Sheldon, A., Sheldon, E., Shen, Y., Shu, Y., Slosar, A., Smea, S.A., Sndden, S.A., Stauffer, F., Steele, O., Strauss, M.A., Streblyanska, A., Suzuki, N., Swanson, M.E.C., Tal, T., Tanaka, M., Thomas, D., Tinker, J.L., Tojeiro, R., Tremonti, C.A., Vargas Magaña, M., Verde, L., Viel, M., Wake, D.A., Watson, M., Weaver, B.A., Weinberg, D.H., Weiner, B.J., West, A.A., White, M., Wood-Vasey, W.M., Yeche, C., Zehavi, I., Zhao, G.B., Zheng, Z., 2013. The Baryon Oscillation Spectroscopic Survey of SDSS-III. *AJ* 145, 10. doi:[10.1088/0004-6256/145/1/10](https://doi.org/10.1088/0004-6256/145/1/10), [arXiv:1208.0022](https://arxiv.org/abs/1208.0022).
- Delgado, A.M., Wadekar, D., Hadzhiyska, B., Bose, S., Hernquist, L., Ho, S., 2022. Modelling the galaxy–halo connection with machine learning. *Mon. Not. Roy. Astron. Soc.* 515, 2733–2746. doi:[10.1093/mnras/stac1951](https://doi.org/10.1093/mnras/stac1951), [arXiv:2111.02422](https://arxiv.org/abs/2111.02422).
- DeRose, J., Wechsler, R.H., Tinker, J.L., Becker, M.R., Mao, Y.Y., McClintock, T., McLaughlin, S., Rozo, E., Zhai, Z., 2019. The AEMULUS Project. I. Numerical Simulations for Precision Cosmology. *ApJ* 875, 69. doi:[10.3847/1538-4357/ab1085](https://doi.org/10.3847/1538-4357/ab1085), [arXiv:1804.05865](https://arxiv.org/abs/1804.05865).
- DESI Collaboration, Aghamousa, A., Aguilar, J., Ahlen, S., Alam, S., Allen, L.E., Allende Prieto, C., Annis, J., Bailey, S., Ballard, C., Ballester, O., Baltay, C., Beaufore, L., Bebek, C., Beers, T.C., Bell, E.F., Bernal, J.L., Besuner, R., Beutler, F., Blake, C., Bleuler, H., Blomqvist, M., Blum, R., Bolton, A.S., Brinceno, C., Brooks, D., Brownstein, J.R., Buckley-Geer, E., Burden, A., Burtin, E., Busca, N.G., Cahn, R.N., Cai, Y.C., Cardiel-Sas, L., Carlberg, R.G., Carton, P.H., Casas, R., Castander, F.J., Cervantes-Cota, J.L., Claybaugh, T.M., Close, M., Coker, C.T., Cole, S., Comparat, J., Cooper, A.P., Cousinou, M.C., Crocce, M., Cuby, J.G., Cunningham, D.P., Davis, T.M., Dawson, K.S., de la Macorra, A., De Vicente, J., Delubac, T., Derwent, M., Dey, A., Dhungana, G., Ding, Z., Doel, P., Duan, Y.T., Ealet, A., Edelstein, J., Eftekharzadeh, S., Eisenstein, D.J., Elliott, A., Escoffier, S., Evatt, M., Fagrellius, P., Fan, X., Fanning, K., Farahi, A., Farhi, J., Favole, G., Feng, Y., Fernandez, E., Findlay, J.R., Finkbeiner, D.P., Fitzpatrick, M.J., Flaughner, B., Flender, S., Font-Ribera, A., Forero-Romero, J.E., Fosalba, P., Frenk, C.S., Fumagalli, M., Gaensicke, B.T., Gallo, G., Garcia-Bellido, J., Gaztanaga, E., Pietro Gentile Fusillo, N., Gerard, T., Gershkovich, I., Giannantonio, T., Gillet, D., Gonzalez-de-Rivera, G., Gonzalez-Perez, V., Gott, S., Graur, O., Gutierrez, G., Guy, J., Habib, S., Heetderks, H., Heetderks, I., Heitmann, K., Hellwing, W.A., Herrera, D.A., Ho, S., Holland, S., Honscheid, K., Huff, E., Hutchinson, T.A., Huterer, D., Hwang, H.S., Illa Laguna, J.M., Ishikawa, Y., Jacobs, D., Jeffrey, N., Jelinsky, P., Jennings, E., Jiang, L., Jimenez, J., Johnson, J., Joyce, R., Jullo, E., Juneau, S., Kama, S., Karcher, A., Karkar, S., Kehoe, R., Kenamer, N., Kent, S., Kilbinger, M., Kim, A.G., Kirkby, D., Kisner, T., Kitandis, E., Kneib, J.P., Kopesov, S., Kovacs, E., Koyama, K., Kremin, A., Kron, R., Kronig, L., Kueter-Young, A., Lacey, C.G., Lafever, R., Lahav, O., Lambert, A., Lampton, M., Landriau, M., Lang, D., Lauer, T.R., Le Goff, J.M., Le Guillou, L., Le Van Suu, A., Lee, J.H., Lee, S.J., Leitner, D., Lesser, M., Levi, M.E., L’Huillier, B., Li, B., Liang, M., Lin, H., Linder, E., Loebman, S.R., Lukić, Z., Ma, J., MacCrann, N., Magneville, C., Makarem, L., Manera, M., Manser, C.J., Marshall, R., Martini, P., Massey, R., Matheo, T., McCauley, J., McDonald, P., McGreer, I.D., Meisner, A., Metcalfe, N., Miller, T.N., Miquel, R., Moustakas, J., Myers, A., Naik, M., Newman, J.A., Nichol, R.C., Nicola, A., Nicolati da Costa, L., Nie, J., Niz, G., Norberg, P., Nord, B., Norman, D., Nugent, P., O’Brien, T., Oh, M., Olsen, K.A.G., Padilla, C., Padmanabhan, H., Padmanabhan, N., Palanque-Delabrouille, N., Palmese, A., Pappalardo, D., Pâris, I., Park, C., Patej, A., Peacock, J.A., Peiris, H.V., Peng, X., Percival, W.J., Perruchot, S., Pieri, M.M., Pogge, R., Pollack, J.E., Poppett, C., Prada, F., Prakash, A., Probst, R.G., Rabinowitz, D., Raichoor, A., Ree, C.H., Refregier, A., Regal, X., Reid, B., Reil, K., Rezaie, M., Rockosi, C.M., Roe, N., Ronayette, S., Roodman, A., Ross, A.J., Ross, N.P., Rossi, G., Rozo, E., Ruhlmann-Kleider, V., Rykoff, E.S., Sabiu, C., Samushia, L., Sanchez, E., Sanchez, J., Schlegel, D.J., Schneider, M., Schubnell, M., Secroun, A., Seljak, U., Seo, H.J., Serrano, S., Shafieloo, A., Shan, H., Sharples, R., Sholl, M.J., Shourt, W.V., Silber, J.H., Silva, D.R., Sirk, M.M., Slosar, A., Smith, A., Smoot, G.F., Som, D., Song, Y.S., Sprayberry, D., Staten, R., Stefanik, A., Tarle, G., Sien Tie, S., Tinker, J.L., Tojeiro, R., Valdes, F., Valenzuela, O., Valluri, M., Vargas-Magana, M., Verde, L., Walker, A.R., Wang, J., Wang, Y., Weaver, B.A., Weaverdyck, C., Wechsler, R.H., Weinberg, D.H., White, M., Yang, Q., Yeche, C., Zhang, T., Zhao, G.B., Zheng, Y., Zhou, X., Zhou, Z., Zhu, Y., Zou, H., Zu, Y., 2016. The DESI Experiment Part I: Science, Targeting, and Survey Design. *arXiv e-prints*, [arXiv:1611.00036doi:10.48550/arXiv.1611.00036](https://arxiv.org/abs/1611.00036doi:10.48550/arXiv.1611.00036), [arXiv:1611.00036](https://arxiv.org/abs/1611.00036).
- Dubois, Y., Peirani, S., Pichon, C., Devriendt, J., Gavazzi, R., Welker, C., Volonteri, M., 2016. The HORIZON-AGN simulation: morphological diversity of galaxies promoted by AGN feedback. *MNRAS* 463, 3948–3964. doi:[10.1093/mnras/stw2265](https://doi.org/10.1093/mnras/stw2265), [arXiv:1606.03086](https://arxiv.org/abs/1606.03086).
- Dubois, Y., Pichon, C., Welker, C., Le Borgne, D., Devriendt, J., Laigle, C., Codis, S., Pogosyan, D., Arnouts, S., Benabed, K., Bertin, E., Blaizot, J., Bouchet, F., Cardoso, J.F., Colombi, S., de Lapparent, V., Desjacques, V., Gavazzi, R., Kassin, S., Kimm, T., McCracken, H., Milliard, B., Peirani, S., Prunet, S., Rouberol, S., Silk, J., Slyz, A., Sousbie, T., Teyssier, R., Tresse, L., Treyer, M., Vibert, D., Volonteri, M., 2014. Dancing in the dark: galactic properties trace spin swings along the cosmic web. *MNRAS* 444, 1453–1468. doi:[10.1093/mnras/stu1227](https://doi.org/10.1093/mnras/stu1227), [arXiv:1402.1165](https://arxiv.org/abs/1402.1165).
- Dumerchat, T., Bautista, J., 2023. Galaxy clustering multi-scale emulation. *arXiv e-prints*, [arXiv:2311.10425doi:10.48550/arXiv.2311.10425](https://arxiv.org/abs/2311.10425doi:10.48550/arXiv.2311.10425), [arXiv:2311.10425](https://arxiv.org/abs/2311.10425).
- Euclid Collaboration, Scaramella, R., Amiaux, J., Mellier, Y., Burigana, C., Carvalho, C.S., Cuillandre, J.C., Da Silva, A., Derosa, A., Dinis, J., Maiorano, E., Maris, M., Tereno, I., Laureijs, R., Boenke, T., Buenadicha, G., Dupac, X., Gaspar Venancio, L.M., Gómez-Álvarez, P., Hoar, J., Lorenzo Alvarez, J., Racca, G.D., Saavedra-Criado, G., Schwartz, J., Vavrek, R., Schirmer, M., Aussel, H., Azzollini, R., Cardone, V.F., Cropper, M., Ealet, A., Garilli, B., Gillard, W., Granett, B.R., Guzzo, L., Hoekstra, H., Jahnke, K., Kitching, T., Maciaszek, T., Meneghetti, M., Miller, L., Nakajima, R., Niemi, S.M., Pasian, F., Percival, W.J., Pottinger, S., Sauvage, M., Scodreggio, M., Wächter, S., Zacchei, A., Aghanim, N., Amara, A., Auphan, T., Auricchio, N., Awan, S., Balestra, A., Bender, R., Bodendorf, C., Bonino, D., Branchini, E., Brau-Nogue, S., Brescia, M., Candini, G.P., Capobianco, V., Carbone, C., Carlberg, R.G., Carretero, J., Casas, R., Castander, F.J., Castellano, M., Cavuoti, S., Cimatti, A., Cledassou, R., Congedo, G., Conselice, C.J., Conversi, L., Copin, Y., Corcione, L., Costille, A., Courbin, F., Degaudenzi, H., Douspis, M., Dubath, F., Duncan, C.A.J., Dusini, S., Farrens, S., Ferriol, S., Fosalba, P., Fourmanoit, N., Frailis, M., Franceschi, E., Franzetti, P., Fumana, M., Gillis, B., Giocoli, C., Grazian, A., Grupp, F., Haugan, S.V.H., Holmes, W., Hormuth, F., Hudelot, P., Kermiche, S., Kiessling, A., Kilbinger, M., Kohley, R., Kubik, B., Kümmel, M., Kunz, M., Kurki-Suonio, H., Lahav, O., Ligeri, S., Lilje, P.B., Lloro, I., Mansutti, O., Marggraf, O., Markovic, K., Marulli, F., Massey, R., Maurogordato, S., Melchior, M., Merlin, E., Meylan, G., Mohr, J.J., Moresco, M., Morin, B., Moscardini, L., Munari, E., Nichol, R.C., Padilla, C., Paltani, S., Peacock, J., Pedersen, K., Pettorino, V., Pires, S., Poncet, M., Popa, L., Pozzetti, L., Raison, F., Rebolo, R., Rhodes, J., Rix, H.W., Roncarelli, M., Rossetti, E., Saglia, R., Schneider, P., Schrabback, T., Secroun, A., Seidel, G., Serrano, S., Sirignano, C., Sirri, G., Skottfelt, J., Stanco, L., Starck, J.L., Tallada-Crespí, P., Tavagnacco, D., Taylor, A.N., Teplitz, H.I., Toledo-Moreo, R., Torradeflot, F., Trifoglio, M., Valentijn, E.A., Valenziano, L., Verdoes Kleijn, G.A., Wang, Y., Welikala, N., Weller, J., Wetzstein, M., Zamorani, G., Zoubian, J., Andreon, S., Baldi, M., Bardelli, S., Boucaud, A., Camera, S., Di Ferdinando, D., Fabbian, G., Farinelli, R., Galeotti, S., Graciá-Carpio, J., Maino, D., Medinaceli, E., Mei, S., Neisser, C., Polenta, G., Renzi, A., Romelli, E., Rosset, C., Sureau, F., Tenti, M., Vassallo, T.,

- Zucca, E., Baccigalupi, C., Balaguera-Antolínez, A., Battaglia, P., Biviano, A., Borgani, S., Bozzo, E., Cabanac, R., Cappi, A., Casas, S., Castignani, G., Colodro-Conde, C., Coupon, J., Courtois, H.M., Cuby, J., de la Torre, S., Desai, S., Dole, H., Fabricius, M., Farina, M., Ferreira, P.G., Finelli, F., Flose-Reimberg, P., Fotopoulou, S., Ganga, K., Gozaliasl, G., Hook, I.M., Keihanen, E., Kirkpatrick, C.C., Liebing, P., Lindholm, V., Mainetti, G., Martinelli, M., Martinet, N., Maturi, M., McCracken, H.J., Metcalf, R.B., Morgante, G., Nightingale, J., Nucita, A., Patrizii, L., Potter, D., Riccio, G., Sánchez, A.G., Sapon, D., Schewtschenko, J.A., Schultheis, M., Scottez, V., Teyssier, R., Tutusaus, I., Valiviita, J., Viel, M., Vriend, W., Whittaker, L., 2022. Euclid preparation. I. The Euclid Wide Survey. *A&A* 662, A112. doi:[10.1051/0004-6361/202141938](https://doi.org/10.1051/0004-6361/202141938), [arXiv:2108.01201](https://arxiv.org/abs/2108.01201).
- Favole, G., Granett, B.R., Silva Lafaunie, J., Sapon, D., 2021. Does jackknife scale really matter for accurate large-scale structure covariances? *MNRAS* 505, 5833–5845. doi:[10.1093/mnras/stab1720](https://doi.org/10.1093/mnras/stab1720), [arXiv:2004.13436](https://arxiv.org/abs/2004.13436).
- Foreman-Mackey, D., Hogg, D.W., Lang, D., Goodman, J., 2013. emcee: The MCMC Hammer. *PASP* 125, 306. doi:[10.1086/670067](https://doi.org/10.1086/670067), [arXiv:1202.3665](https://arxiv.org/abs/1202.3665).
- Fosalba, P., Gaztañaga, E., Castander, F.J., Crocce, M., 2015. The MICE Grand Challenge light-cone simulation - III. Galaxy lensing mocks from all-sky lensing maps. *MNRAS* 447, 1319–1332. doi:[10.1093/mnras/stu2464](https://doi.org/10.1093/mnras/stu2464), [arXiv:1312.2947](https://arxiv.org/abs/1312.2947).
- Friedrich, O., Seitz, S., Eifler, T.F., Gruen, D., 2016. Performance of internal covariance estimators for cosmic shear correlation functions. *MNRAS* 456, 2662–2680. doi:[10.1093/mnras/stv2833](https://doi.org/10.1093/mnras/stv2833), [arXiv:1508.00895](https://arxiv.org/abs/1508.00895).
- Garrison, L.H., Eisenstein, D.J., Ferrer, D., Maksimova, N.A., Pinto, P.A., 2021. The ABACUS cosmological N-body code. *MNRAS* 508, 575–596. doi:[10.1093/mnras/stab2482](https://doi.org/10.1093/mnras/stab2482), [arXiv:2110.11392](https://arxiv.org/abs/2110.11392).
- Garrison, L.H., Eisenstein, D.J., Ferrer, D., Metchnik, M.V., Pinto, P.A., 2016. Improving Initial Conditions for Cosmological N-Body Simulations. *Mon. Not. Roy. Astron. Soc.* 461, 4125–4145. doi:[10.1093/mnras/stw1594](https://doi.org/10.1093/mnras/stw1594), [arXiv:1605.02333](https://arxiv.org/abs/1605.02333).
- Garrison, L.H., Eisenstein, D.J., Ferrer, D., Tinker, J.L., Pinto, P.A., Weinberg, D.H., 2018. The Abacus Cosmos: A Suite of Cosmological N-body Simulations. *ApJS* 236, 43. doi:[10.3847/1538-4365/aabfd3](https://doi.org/10.3847/1538-4365/aabfd3), [arXiv:1712.05768](https://arxiv.org/abs/1712.05768).
- Garrison, L.H., Eisenstein, D.J., Pinto, P.A., 2019. A high-fidelity realization of the Euclid code comparison N-body simulation with ABACUS. *MNRAS* 485, 3370–3377. doi:[10.1093/mnras/stz634](https://doi.org/10.1093/mnras/stz634), [arXiv:1810.02916](https://arxiv.org/abs/1810.02916).
- Gómez-Vargas, I., Medel Esquivel, R., García-Salcedo, R., Vázquez, J.A., 2021. Neural network reconstructions for the Hubble parameter, growth rate and distance modulus. *arXiv e-prints*, [arXiv:2104.00595](https://arxiv.org/abs/2104.00595)doi:[10.48550/arXiv.2104.00595](https://doi.org/10.48550/arXiv.2104.00595), [arXiv:2104.00595](https://arxiv.org/abs/2104.00595).
- Gott, J. Richard, I., Vogeley, M.S., Podariu, S., Ratna, B., 2001. Median Statistics, H_0 , and the Accelerating Universe. *ApJ* 549, 1–17. doi:[10.1086/319055](https://doi.org/10.1086/319055), [arXiv:astro-ph/0006103](https://arxiv.org/abs/astro-ph/0006103).
- Hearin, A.P., et al., 2017. Forward Modeling of Large-Scale Structure: An open-source approach with Halotools. *Astron. J.* 154, 190. doi:[10.5281/zenodo.835895](https://doi.org/10.5281/zenodo.835895), [arXiv:1606.04106](https://arxiv.org/abs/1606.04106).
- Heitmann, K., Finkel, H., Pope, A., Morozov, V., Frontiere, N., Habib, S., Rangel, E., Uram, T., Korytov, D., Child, H., Flender, S., Insley, J., Rizzi, S., 2019. The Outer Rim Simulation: A Path to Many-core Supercomputers. *ApJS* 245, 16. doi:[10.3847/1538-4365/ab4da1](https://doi.org/10.3847/1538-4365/ab4da1), [arXiv:1904.11970](https://arxiv.org/abs/1904.11970).
- Hornik, K., 1991. Approximation capabilities of multilayer feedforward networks. *Neural Networks* 4, 251–257. URL: <https://api.semanticscholar.org/CorpusID:7343126>.
- Ishiyama, T., Fukushige, T., Makino, J., 2009. GreeM: Massively Parallel TreePM Code for Large Cosmological N-body Simulations. *PASJ* 61, 1319. doi:[10.1093/pasj/61.6.1319](https://doi.org/10.1093/pasj/61.6.1319), [arXiv:0910.0121](https://arxiv.org/abs/0910.0121).
- Jing, Y.P., Mo, H.J., Börner, G., 1998. Spatial Correlation Function and Pairwise Velocity Dispersion of Galaxies: Cold Dark Matter Models versus the Las Campanas Survey. *ApJ* 494, 1–12. doi:[10.1086/305209](https://doi.org/10.1086/305209), [arXiv:astro-ph/9707106](https://arxiv.org/abs/astro-ph/9707106).
- Klypin, A., Yepes, G., Gottlöber, S., Prada, F., Heß, S., 2016. Multi-Dark simulations: the story of dark matter halo concentrations and density profiles. *MNRAS* 457, 4340–4359. doi:[10.1093/mnras/stw248](https://doi.org/10.1093/mnras/stw248), [arXiv:1411.4001](https://arxiv.org/abs/1411.4001).
- Landy, S.D., Szalay, A.S., 1993. Bias and Variance of Angular Correlation Functions. *ApJ* 412, 64. doi:[10.1086/172900](https://doi.org/10.1086/172900).
- Lucie-Smith, L., Peiris, H.V., Pontzen, A., Lochner, M., 2018. Machine learning cosmological structure formation. *MNRAS* 479, 3405–3414. doi:[10.1093/mnras/sty1719](https://doi.org/10.1093/mnras/sty1719), [arXiv:1802.04271](https://arxiv.org/abs/1802.04271).
- MacKay, D.J.C., 1992. Bayesian interpolation. *Neural Computation* 4, 415–447. URL: <https://api.semanticscholar.org/CorpusID:1762283>.
- Maksimova, N.A., Garrison, L.H., Eisenstein, D.J., Hadzhiyska, B., Bose, S., Satterthwaite, T.P., 2021. ABACUSSUMMIT: a massive set of high-accuracy, high-resolution N-body simulations. *MNRAS* 508, 4017–4037. doi:[10.1093/mnras/stab2484](https://doi.org/10.1093/mnras/stab2484), [arXiv:2110.11398](https://arxiv.org/abs/2110.11398).
- McCarthy, I.G., Schaye, J., Bird, S., Le Brun, A.M.C., 2017. The BAHAMAS project: calibrated hydrodynamical simulations for large-scale structure cosmology. *MNRAS* 465, 2936–2965. doi:[10.1093/mnras/stw2792](https://doi.org/10.1093/mnras/stw2792), [arXiv:1603.02702](https://arxiv.org/abs/1603.02702).
- Meng Loh, J., 2008. A valid and fast spatial bootstrap for correlation functions. *arXiv e-prints*, [arXiv:0805.2325](https://arxiv.org/abs/0805.2325)doi:[10.48550/arXiv.0805.2325](https://doi.org/10.48550/arXiv.0805.2325), [arXiv:0805.2325](https://arxiv.org/abs/0805.2325).
- Metchnik, M.V.L., 2009. A fast N-body scheme for computational cosmology. Ph.D. thesis. University of Arizona.
- Mohammad, F.G., Percival, W.J., 2022. Creating jackknife and bootstrap estimates of the covariance matrix for the two-point correlation function. *MNRAS* 514, 1289–1301. doi:[10.1093/mnras/stac1458](https://doi.org/10.1093/mnras/stac1458), [arXiv:2109.07071](https://arxiv.org/abs/2109.07071).
- Mucesh, S., Hartley, W.G., Palmese, A., Lahav, O., Whiteway, L., Bluck, A.F.L., Alarcon, A., Amon, A., Bechtol, K., Bernstein, G.M., Carnero Rosell, A., Carrasco Kind, M., Choi, A., Eckert, K., Everett, S., Gruen, D., Gruendl, R.A., Harrison, I., Huff, E.M., Kuropatkin, N., Sevilla-Noarbe, I., Sheldon, E., Yanny, B., Aguena, M., Allam, S., Bacon, D., Bertin, E., Bhargava, S., Brooks, D., Carretero, J., Castander, F.J., Conselice, C., Costanzi, M., Crocce, M., da Costa, L.N., Pereira, M.E.S., De Vicente, J., Desai, S., Diehl, H.T., Drlica-Wagner, A., Evrard, A.E., Ferrero, I., Flaugher, B., Fosalba, P., Frieman, J., García-Bellido, J., Gaztanaga, E., Gerdes, D.W., Gschwend, J., Gutierrez, G., Hinton, S.R., Hollowood, D.L., Honscheid, K., James, D.J., Kuehn, K., Lima, M., Lin, H., Maia, M.A.G., Melchior, P., Menanteau, F., Miquel, R., Morgan, R., Paz-Chinchón, F., Plazas, A.A., Sanchez, E., Scarpine, V., Schubnell, M., Serrano, S., Smith, M., Suchyta, E., Tarle, G., Thomas, D., To, C., Varga, T.N., Wilkinson, R.D., DES Collaboration, 2021. A machine learning approach to galaxy properties: joint redshift-stellar mass probability distributions with Random Forest. *MNRAS* 502, 2770–2786. doi:[10.1093/mnras/stab164](https://doi.org/10.1093/mnras/stab164), [arXiv:2012.05928](https://arxiv.org/abs/2012.05928).
- Nadler, E.O., Mao, Y.Y., Wechsler, R.H., Garrison-Kimmel, S., Wetzel, A., 2018. Modeling the Impact of Baryons on Subhalo Populations with Machine Learning. *ApJ* 859, 129. doi:[10.3847/1538-4357/aac266](https://doi.org/10.3847/1538-4357/aac266), [arXiv:1712.04467](https://arxiv.org/abs/1712.04467).
- Nelson, D., Pillepich, A., Genel, S., Vogelsberger, M., Springel, V., Torrey, P., Rodriguez-Gomez, V., Sijacki, D., Snyder, G.F., Griffen, B., Marinacci, F., Blecha, L., Sales, L., Xu, D., Hernquist, L., 2015. The illustris simulation: Public data release. *Astronomy and Computing* 13, 12–37. doi:[10.1016/j.ascom.2015.09.003](https://doi.org/10.1016/j.ascom.2015.09.003), [arXiv:1504.00362](https://arxiv.org/abs/1504.00362).
- Nelson, D., Springel, V., Pillepich, A., Rodriguez-Gomez, V., Torrey, P., Genel, S., Vogelsberger, M., Pakmor, R., Marinacci, F., Weinberger, R., Kelley, L., Lovell, M., Diemer, B., Hernquist, L., 2019. The IllustrisTNG simulations: public data release. *Computational Astrophysics and Cosmology* 6, 2. doi:[10.1186/s40668-019-0028-x](https://doi.org/10.1186/s40668-019-0028-x), [arXiv:1812.05609](https://arxiv.org/abs/1812.05609).
- Norberg, P., Baugh, C.M., Gaztañaga, E., Croton, D.J., 2009. Statistical analysis of galaxy surveys - I. Robust error estimation for two-point clustering statistics. *MNRAS* 396, 19–38. doi:[10.1111/j.1365-2966.2009.14389.x](https://doi.org/10.1111/j.1365-2966.2009.14389.x), [arXiv:0810.1885](https://arxiv.org/abs/0810.1885).
- Ntampaka, M., Eisenstein, D.J., Yuan, S., Garrison, L.H., 2020. A Hybrid Deep Learning Approach to Cosmological Constraints from Galaxy Redshift Surveys. *ApJ* 889, 151. doi:[10.3847/1538-4357/ab5f5e](https://doi.org/10.3847/1538-4357/ab5f5e), [arXiv:1909.10527](https://arxiv.org/abs/1909.10527).
- Nygaard, A., Holm, E.B., Hannestad, S., Tram, T., 2023. CONNECT: a neural network based framework for emulating cosmological observables and cosmological parameter inference. *J. Cosmology Astropart. Phys.* 2023, 025. doi:[10.1088/1475-7516/2023/05/025](https://doi.org/10.1088/1475-7516/2023/05/025), [arXiv:2205.15726](https://arxiv.org/abs/2205.15726).
- Peacock, J.A., Smith, R.E., 2000. Halo occupation numbers and galaxy bias. *MNRAS* 318, 1144–1156. doi:[10.1046/j.1365-8711.2000.03779.x](https://doi.org/10.1046/j.1365-8711.2000.03779.x), [arXiv:astro-ph/0005010](https://arxiv.org/abs/astro-ph/0005010).
- Pedregosa, F., Varoquaux, G., Gramfort, A., Michel, V., Thirion, B., Grisel, O., Blondel, M., Müller, A., Nothman, J., Louppe, G., Prettenhofer, P., Weiss, R., Dubourg, V., Vanderplas, J., Passos, A., Cournapeau, D., Brucher, M., Perrot, M., Duchesnay, É., 2011. Scikit-learn: Machine Learning in Python. *Journal of Machine Learning Research* 12, 2825–2830. doi:[10.48550/](https://doi.org/10.48550/)

- [arXiv:1201.0490](#), [arXiv:1201.0490](#).
- Perez, L.A., Genel, S., Villaescusa-Navarro, F., Somerville, R.S., Gabrielpilai, A., Anglés-Alcázar, D., Wandelt, B.D., Yung, L.Y.A., 2023. Constraining Cosmology with Machine Learning and Galaxy Clustering: The CAMELS-SAM Suite. *ApJ* 954, 11. doi:[10.3847/1538-4357/accd52](#), [arXiv:2204.02408](#).
- Potter, D., Stadel, J., Teyssier, R., 2017. PKDGRAV3: beyond trillion particle cosmological simulations for the next era of galaxy surveys. *Computational Astrophysics and Cosmology* 4, 2. doi:[10.1186/s40668-017-0021-1](#), [arXiv:1609.08621](#).
- Prechelt, L., 1998. Automatic early stopping using cross validation: quantifying the criteria. *Neural networks : the official journal of the International Neural Network Society* 11 4, 761–767. URL: <https://api.semanticscholar.org/CorpusID:2887064>.
- Probst, P., Wright, M., Boulesteix, A.L., 2018. Hyperparameters and Tuning Strategies for Random Forest. *arXiv e-prints*, arXiv:1804.03515doi:[10.48550/arXiv.1804.03515](#), [arXiv:1804.03515](#).
- Rumelhart, D.E., Hinton, G.E., Williams, R.J., 1986. Learning representations by back-propagating errors. *Nature* 323, 533–536. doi:[10.1038/323533a0](#).
- Schaye, J., Crain, R.A., Bower, R.G., Furlong, M., Schaller, M., Theuns, T., Dalla Vecchia, C., Frenk, C.S., McCarthy, I.G., Helly, J.C., Jenkins, A., Rosas-Guevara, Y.M., White, S.D.M., Baes, M., Booth, C.M., Camps, P., Navarro, J.F., Qu, Y., Rahmati, A., Sawala, T., Thomas, P.A., Trayford, J., 2015. The EAGLE project: simulating the evolution and assembly of galaxies and their environments. *MNRAS* 446, 521–554. doi:[10.1093/mnras/stu2058](#), [arXiv:1407.7040](#).
- Schmidhuber, J., 2014. Deep Learning in Neural Networks: An Overview. *arXiv e-prints*, arXiv:1404.7828doi:[10.48550/arXiv.1404.7828](#), [arXiv:1404.7828](#).
- Scoccimarro, R., Sheth, R.K., Hui, L., Jain, B., 2001. How Many Galaxies Fit in a Halo? Constraints on Galaxy Formation Efficiency from Spatial Clustering. *ApJ* 546, 20–34. doi:[10.1086/318261](#), [arXiv:astro-ph/0006319](#).
- Seljak, U., 2000. Analytic model for galaxy and dark matter clustering. *MNRAS* 318, 203–213. doi:[10.1046/j.1365-8711.2000.03715.x](#), [arXiv:astro-ph/0001493](#).
- Sinha, M., Garrison, L.H., 2020. CORRFUNC - a suite of blazing fast correlation functions on the CPU. *MNRAS* 491, 3022–3041. doi:[10.1093/mnras/stz3157](#).
- Sinha, M., Garrison, L.H., 2020. corrfunc - a suite of blazing fast correlation functions on the CPU. *Mon. Not. Roy. Astron. Soc.* 491, 3022–3041. doi:[10.1093/mnras/stz3157](#), [arXiv:1911.03545](#).
- Spergel, D., Gehrels, N., Baltay, C., Bennett, D., Brekinridge, J., Donahue, M., Dressler, A., Gaudi, B.S., Greene, T., Guyon, O., Hirata, C., Kalirai, J., Kasdin, N.J., Macintosh, B., Moos, W., Perlmutter, S., Postman, M., Rauscher, B., Rhodes, J., Wang, Y., Weinberg, D., Benford, D., Hudson, M., Jeong, W.S., Mellier, Y., Traub, W., Yamada, T., Capak, P., Colbert, J., Masters, D., Penny, M., Savransky, D., Stern, D., Zimmerman, N., Barry, R., Bartusek, L., Carpenter, K., Cheng, E., Content, D., Dekens, F., Demers, R., Grady, K., Jackson, C., Kuan, G., Kruk, J., Melton, M., Nemati, B., Parvin, B., Poberezhskiy, I., Peddie, C., Ruffa, J., Wallace, J.K., Whipple, A., Wollack, E., Zhao, F., 2015. Wide-Field Infrared Survey Telescope-Astrophysics Focused Telescope Assets WFIRST-AFTA 2015 Report. *arXiv e-prints*, arXiv:1503.03757doi:[10.48550/arXiv.1503.03757](#), [arXiv:1503.03757](#).
- Springel, V., 2005. The cosmological simulation code GADGET-2. *MNRAS* 364, 1105–1134. doi:[10.1111/j.1365-2966.2005.09655.x](#), [arXiv:astro-ph/0505010](#).
- Springel, V., 2010. E pur si muove: Galilean-invariant cosmological hydrodynamical simulations on a moving mesh. *MNRAS* 401, 791–851. doi:[10.1111/j.1365-2966.2009.15715.x](#), [arXiv:0901.4107](#).
- Springel, V., Pakmor, R., Zier, O., Reinecke, M., 2021. Simulating cosmic structure formation with the GADGET-4 code. *MNRAS* 506, 2871–2949. doi:[10.1093/mnras/stab1855](#), [arXiv:2010.03567](#).
- Springel, V., Yoshida, N., White, S.D.M., 2001. GADGET: a code for collisionless and gasdynamical cosmological simulations. *New A* 6, 79–117. doi:[10.1016/S1384-1076\(01\)00042-2](#), [arXiv:astro-ph/0003162](#).
- Srivastava, N., Hinton, G.E., Krizhevsky, A., Sutskever, I., Salakhutdinov, R., 2014. Dropout: a simple way to prevent neural networks from overfitting. *J. Mach. Learn. Res.* 15, 1929–1958. URL: <https://api.semanticscholar.org/CorpusID:6844431>.
- Teyssier, R., 2002. Cosmological hydrodynamics with adaptive mesh refinement. A new high resolution code called RAMSES. *A&A* 385, 337–364. doi:[10.1051/0004-6361:20011817](#), [arXiv:astro-ph/0111367](#).
- Theodoridis, S., 2015. Machine learning: a Bayesian and optimization perspective. Academic press.
- Wadekar, D., Villaescusa-Navarro, F., Ho, S., Perreault-Levasseur, L., 2020. Modeling assembly bias with machine learning and symbolic regression. *arXiv e-prints*, arXiv:2012.00111doi:[10.48550/arXiv.2012.00111](#), [arXiv:2012.00111](#).
- Willmott, C., Matsuura, K., 2005. Advantages of the mean absolute error (MAE) over the root mean square error (RMSE) in assessing average model performance. *Climate Research* 30, 79–82. doi:[10.3354/cr030079](#).
- Xu, X., Ho, S., Trac, H., Schneider, J., Poczos, B., Ntampaka, M., 2013. A First Look at creating mock catalogs with machine learning techniques. *Astrophys. J.* 772, 147. doi:[10.1088/0004-637X/772/2/147](#), [arXiv:1303.1055](#).
- Xu, X., Kumar, S., Zehavi, I., Contreras, S., 2021. Predicting halo occupation and galaxy assembly bias with machine learning. *MNRAS* 507, 4879–4899. doi:[10.1093/mnras/stab2464](#), [arXiv:2107.01223](#).
- Zehavi, I., Contreras, S., Padilla, N., Smith, N.J., Baugh, C.M., Norberg, P., 2018. The Impact of Assembly Bias on the Galaxy Content of Dark Matter Halos. *ApJ* 853, 84. doi:[10.3847/1538-4357/aaa54a](#), [arXiv:1706.07871](#).
- Zheng, Z., Berlind, A.A., Weinberg, D.H., Benson, A.J., Baugh, C.M., Cole, S., Davé, R., Frenk, C.S., Katz, N., Lacey, C.G., 2005. Theoretical Models of the Halo Occupation Distribution: Separating Central and Satellite Galaxies. *ApJ* 633, 791–809. doi:[10.1086/466510](#), [arXiv:astro-ph/0408564](#).
- Zheng, Z., Coil, A.L., Zehavi, I., 2007. Galaxy Evolution from Halo Occupation Distribution Modeling of DEEP2 and SDSS Galaxy Clustering. *ApJ* 667, 760–779. doi:[10.1086/521074](#), [arXiv:astro-ph/0703457](#).
- Zheng, Z., Zehavi, I., Eisenstein, D.J., Weinberg, D.H., Jing, Y.P., 2009. Halo Occupation Distribution Modeling of Clustering of Luminous Red Galaxies. *ApJ* 707, 554–572. doi:[10.1088/0004-637X/707/1/554](#), [arXiv:0809.1868](#).

Appendix A. Machine Learning Overview

We used supervised machine-learning techniques for regression to model the dependence of small-scale clustering measurements on HOD parameters. Specifically, we tested and compared three different regression algorithms – ANN, RF, and BR regression.

Appendix A.1. Artificial Neural Networks

Artificial neural networks (ANNs) are computing systems inspired by biological neural networks, designed to identify complex patterns in data. They consist of an input layer, one or more hidden layers, and an output layer, each containing neuron-like processing units connected by synaptic weights (Schmidhuber, 2014). By tuning these weights through backpropagation, ANNs can approximate complex functions (Rumelhart et al., 1986; Hornik, 1991).

We implement ANNs using MLPRegressor in Scikit-Learn, a fully-connected feedforward network. The HOD parameters were input features and clustering measurements were the output. Using Hyperparameter tuning we determine the optimal parameters like the number of layers/nodes, activation function, solver, and regularization. Activation functions like “ReLU” and “tanh” were considered. To prevent overfitting, we used early stopping based on a validation set and dropout regularization (Prechelt, 1998; Srivastava et al., 2014).

Appendix A.2. Random Forest Regression

Random forest (RF) aggregates predictions from decision trees trained on randomized data subsets, which improves generalization and reduces overfitting (Breiman, 2001; Biau and Scornet, 2015). RF regression averages predictions over all trees

$$\hat{y}_{\text{RF}} = \frac{1}{B} \sum_{b=1}^B \hat{y}_b, \quad (\text{A.1})$$

where \hat{y}_b is the b^{th} tree's prediction. We use RandomForestRegressor in Scikit-Learn with hyperparameter tuning (Probst et al., 2018). It is known for its scalability, ability to handle high-dimensional data, and resistance to noise and outliers. While capable of handling large datasets, RF may become computationally expensive as the number of trees or features increases.

Appendix A.3. Ridge Regression (BR)

Ridge regression regularizes linear regression by penalizing the residual sum of squares

$$L(\beta) = \sum_{i=1}^n (y_i - \mathbf{x}_i \beta)^2 + \lambda |\beta|^2. \quad (\text{A.2})$$

The λ hyperparameter controls regularization strength. This shrinks coefficients to prevent overfitting. We used BayesianRidge in Scikit-Learn, which estimates the regularization hyperparameter (λ) in a Bayesian framework (MacKay, 1992). Ridge regression is similar to LASSO but uses L2 regularization.

Ridge regression is commonly fitted using coordinate descent optimization algorithms. This involves iteratively minimizing the objective function along each coordinate direction while holding other coefficients fixed. The coordinate direction that leads to the largest improvement in the objective is selected in each iteration. This continues until convergence when changes along any coordinate cease to decrease the objective further.

Appendix B. Evaluating Machine Learning Model

We evaluated our machine learning regression models using several numerical measures that quantify the difference between predicted (\hat{y}_i) and actual (y_i) values. These accuracy metrics provided insight into model performance and aided in selecting the best approach.

Appendix B.1. Mean Squared Error

The mean squared error (MSE) is computed by taking the average of the squared differences between the predicted and true values

$$MSE = \frac{1}{n} \sum_{i=1}^n (\hat{y}_i - y_i)^2, \quad (\text{B.1})$$

where n is the number of samples.

Squaring the errors has the effect of heavily penalizing large deviations compared to smaller ones. However, this disproportionate penalty also makes MSE very sensitive to outliers that have large errors (Willmott and Matsuura, 2005). MSE ranges from 0 to ∞ , with lower values indicating better model fit.

Appendix B.2. Mean Absolute Error

The mean absolute error (MAE) calculates the average magnitude of errors without squaring

$$MAE = \frac{1}{n} \sum_{i=1}^n |\hat{y}_i - y_i|. \quad (\text{B.2})$$

Taking the absolute value of the differences avoids excessive penalties for large errors. This makes MAE more robust to outliers compared to MSE (Gott et al., 2001; Chai and Draxler, 2014). MAE ranges from 0 to ∞ , with 0 being a perfect fit.

Appendix B.3. R-squared

The R-squared or coefficient of determination is

$$R^2 = 1 - \frac{RSS}{TSS}, \quad (\text{B.3})$$

where RSS is the residual sum of squares

$$RSS = \sum_{i=1}^n (y_i - \hat{y}_i)^2, \quad (\text{B.4})$$

and TSS is the total sum of squares

$$TSS = \sum_{i=1}^n (y_i - \bar{y})^2. \quad (\text{B.5})$$

Here for i^{th} observation, y_i is the actual value, \hat{y}_i is the predicted value and \bar{y} represents the mean of the actual values. R^2 compares the accuracy of the model's predictions to the accuracy of simply predicting the mean in all cases. It indicates the explanatory power of the model. R^2 values range from 0 to 1, with higher values indicating more variance explained by the model.

Appendix B.4. Adjusted R-Squared

The R-squared metric can be adjusted to account for the number of predictors in the model. The adjusted R-squared is defined as

$$R_{adj}^2 = 1 - (1 - R^2) \frac{n - 1}{n - p - 1} \quad (\text{B.6})$$

where n is the sample size and p is the number of explanatory variables in the model.

Unlike regular R^2 , the adjusted R^2 will penalize models for having too many unnecessary predictors. It will always be less than or equal to the unadjusted R^2 . Generally, adding predictors improves the basic R^2 but can worsen the adjusted R^2 if they are redundant. This helps prevent overfitting the training data (Theodoridis, 2015).

For comparing regression models, the adjusted R^2 provides a more conservative estimate that accounts for model complexity. However, it has limitations when the sample size is small or the number of predictors is large relative to the observations.

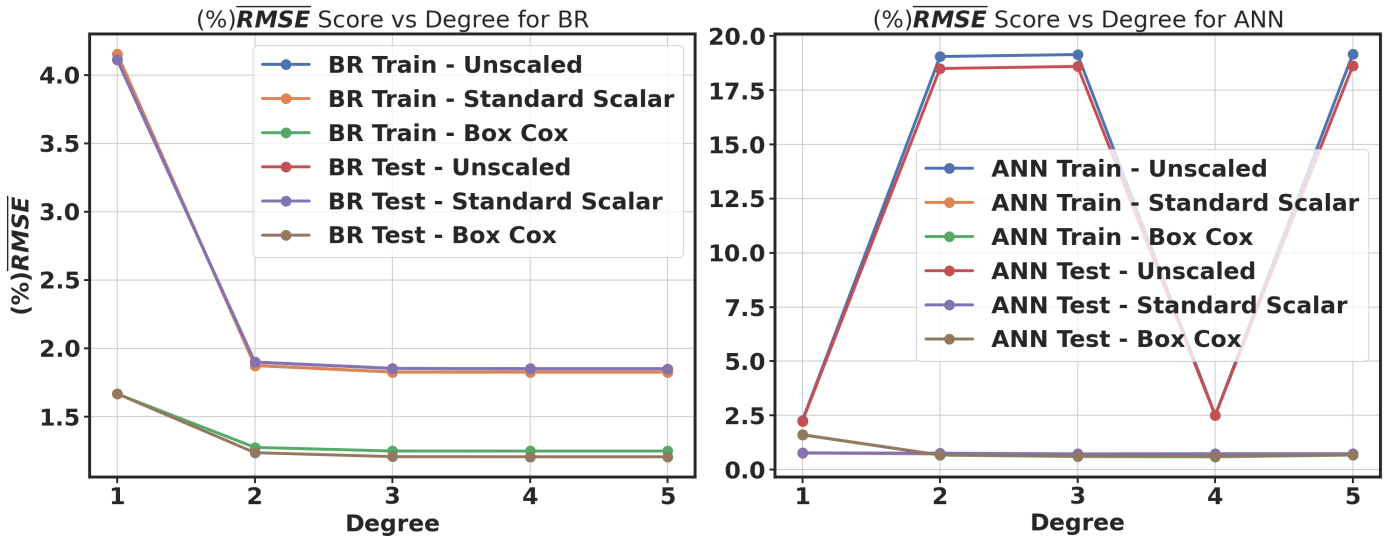


Figure B.13: Comparison of average percent RMSE Scores between unscaled, SC, BC, and YJ on BR and ANN as a function of polynomial features on w_p for the small box train and test set. We calculate the average percent RMSE (see Section 5.6 for definition) as a function of degree polynomial. The left plot shows the average percent RMSE of the BR model. The right plot shows the average percent RMSE of the ANN model.

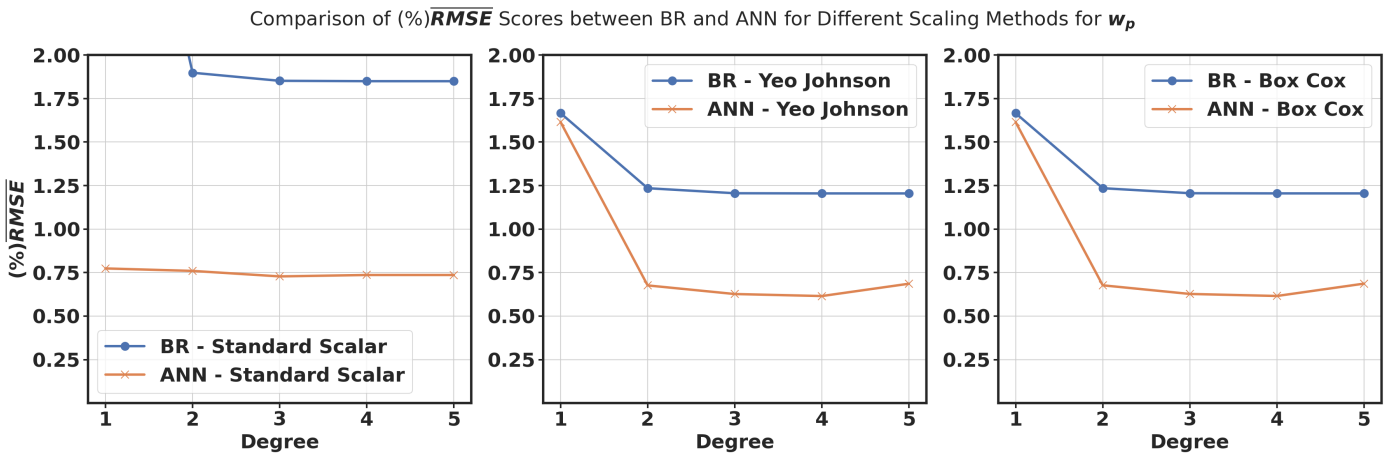


Figure B.14: Comparison of average percent RMSE Scores between BR and ANN for SC, YJ, and BC on w_p test set. The left, middle, and right plot shows the average percent RMSE of SC, YJ, and BC transformations respectively.

Appendix B.5. Choice of Polynomial Features

Using polynomial features we can increase the number of features, capturing non-linear relationships in the data. Although a flexible model like ANN requires minimal preprocessing, incorporating polynomial features can reduce model complexity, leading to faster convergence. The selection of the polynomial degree is pivotal, as escalating it may result in model overfitting.

Fig. B.13 shows the relationship between $(\%) \overline{RMSE}$ and the degree of polynomial on BR and ANN for w_p on the small box. $(\%) \overline{RMSE}$ score decreases with increasing the model complexity but decreases slowly after 2nd order. We opt for a degree of 2, given marginal performance improvements beyond. Interestingly, ANN exhibits inferior performance with raw target data.

Fig. B.14 illustrates the comparison between ANN and BR. This finding aligns with Table 4, demonstrating that ANN outperforms BR at the same degree of polynomial.